https://doi.org/10.5194/egusphere-2025-4123
Preprint. Discussion started: 9 September 2025

Bedrock ledges, colluvial wedges, and ridgetop water towers: Characterizing geomorphic and atmospheric controls on the 2023 Wrangell landslide to inform landslide assessment in Southeast Alaska, USA

Joshua J. Roering*[1], Margaret M. Darrow[2], Annette I. Patton[3], Aaron Jacobs[4]

[1] Department of Earth Sciences, University of Oregon, Eugene, OR, USA
[2] Department of Civil, Geological, and Environmental Engineering, University of Alaska Fairbanks, Fairbanks, AK, USA
[3] College of Forestry, Oregon State University, Corvallis, OR, USA
[4] National Weather Service, Juneau, AK, USA

Correspondence to: Joshua J. Roering (jroering@uoregon.edu)

Abstract. In the past decade, several fatal landslides have impacted Southeast Alaska, highlighting the need to advance our understanding of regional geomorphic and atmospheric controls on triggering events and runout behaviour. A large and long runout landslide on Wrangell Island, with area in the top 0.5% of >14,760 slides mapped in the Tongass National Forest, initiated during an atmospheric river event in November 2023 and travelled >1 km downslope, causing six fatalities. We used field observations, sequential airborne lidar, geotechnical analyses, and climate data to characterize the geomorphic, hydrologic, and atmospheric conditions contributing to the landslide. Rainfall intensities recorded at the Wrangell airport were modest (~1-yr recurrence interval), but rapid snowmelt and drainage from a ridgetop wetland may have contributed to rapid saturation of the landslide. Although strong winds were recorded, we did not observe extensive windthrow, which may downgrade its contribution to slope failure. The landslide mobilized a steep, thick (>4 m) wedge of colluvium that accumulated below a resistant bedrock ledge and entrained additional colluvial deposits as it travelled downslope across cliff-bench topography. The substantial entrainment resulted in an unusually large width, extensive runout, and low depositional slope as the landslide terminated in the coastal environment. Our results suggest that the sequencing of rain- and snow-dominated storms, geologic controls on post-glacial colluvium production and accumulation, and ridgetop hydrology contributed to landslide initiation and mobility. Advances in post-glacial landscape evolution models, frequent lidar acquisition, and additional climate data are needed to inform regional landslide hazard assessment.

1 Introduction

In steep, forested landscapes, shallow landslides serve as the primary agent of erosion (Hovius et al., 1997; Korup et al., 2010; Larsen et al., 2010; Swanson et al., 1987), produce and transport sediment that contributes to aquatic habitat (Geertsema and Pojar, 2007), set the relief structure of mountain ranges (Stock and Dietrich, 2003), and constitute a significant hazard to

https://doi.org/10.5194/egusphere-2025-4123
Preprint. Discussion started: 9 September 2025

proximal communities and infrastructure (Godt et al., 2022). In contrast to bedrock landslides whose failures are governed by bedrock properties (Schuster and Highland, 2001; Wyllie and Mah, 2004), shallow landslides composed of loose, unconsolidated material tend to initiate in zones of thick colluvium that experience variable saturation due to precipitation and snowmelt and in turn generate debris flows or debris slides with significant downslope runout and inundation (Gabet and Mudd, 2006; Iverson, 2000). In unglaciated terrain, these shallow landslides often occur in unchanneled valleys (or hollows) at the upstream tips of valley networks that are subject to cycles of infilling and excavation over 10^2- to 10^4-yr timescales (Benda and Dunne, 1997; Dietrich et al., 1986; D'Odorico and Fagherazzi, 2003). Characteristic ridge-valley sequences in these settings have facilitated the identification and characterization of shallow landslide and debris flow processes and informed models for soil transport, near-surface hydrologic response, and landslide initiation and runout (Dietrich et al., 1995; Lancaster et al., 2003; Montgomery et al., 1997; Reid et al., 2016; Schmidt et al., 2001).

In contrast, in steep, post-glacial settings, terrain morphology tends to be dominated by glacial landforms and deposits such that dissection is patchy and weakly established (Brardinoni and Hassan, 2006). Specifically, shallow landslides tend to initiate within soils of thin-to-moderate thickness (1-3 m) on steep planar slopes and runout to valley floors or low-order channels that are often highly unstable and subject to frequent reorganization (Brardinoni et al., 2009). In these highly dynamic settings, topographic controls on colluvium accumulation along steep, unchanneled slopes is poorly constrained making it difficult to predict landslide entrainment and volumetric growth which largely determine runout and inundation (Brien et al., 2025; Iverson and Ouyang, 2015; Patton et al., 2022). Furthermore, the relative importance of processes that generate the accumulation of colluvium, such as in-situ weathering of till or bedrock, transport of soil or talus deposits, and deposition of allochthonous deposits (e.g., tephra), and thus promote initiation and entrainment is also poorly known (Bovy et al., 2016; Spinola et al., 2024). In these formerly glaciated hillslopes, the lack of a conceptual framework for the production and transport of unconsolidated material inhibits our ability to identify areas susceptible to shallow landsliding, runout, and inundation (Brardinoni et al., 2018; Guthrie, 2002).

The triggering of shallow landslides and debris flows in post-glacial terrain is primarily accomplished by storm events that generate intense rainfall over several hours (Fan et al., 2020; Guthrie et al., 2010; Patton et al., 2023; Swanston, 1969) and shallow subsurface stormflow that saturates colluvium and leads to elevated pore pressures. For example, Patton et al. (2023) used logistic regression and Bayesian methods to demonstrate that 3-hr rainfall intensity can effectively differentiate storms that trigger debris flows near Sitka, Alaska. Their analysis forms the basis of the *sitkalandslide.org* warning system that uses National Weather Service (NWS) forecasts to define the 3-hr rainfall intensity with medium (7 mm hr^{-1}) and high (11 mm hr^{-1}) levels of risk up to 3 days in the future (Lempert et al., 2023). Additional studies also highlight the importance of rain-on-snow events that can rapidly advect large quantities of water into near surface soil and bedrock and contribute to slope instability (Darrow et al., 2022). Field observations from recently failed head scarps reveal evidence for abundant seepage associated with permeability contrasts along the interface between bedrock, till, or colluvium as well as localized flow

https://doi.org/10.5194/egusphere-2025-4123
Preprint. Discussion started: 9 September 2025

associated with fracture networks (Buma and Pawlik, 2021; Swanston, 1970). Notably, the upslope source of shallow groundwater and near-surface runoff that controls hydrologic response in post-glacial steeplands remains unclear owing to the paucity of high-resolution topography, field observations, and instrumental records in these settings. Additional factors contributing to landslide triggering in steep, forested terrain include timber harvest, fire, disease, and infestation, which can affect surface hydraulic properties and root reinforcement that resists sliding (Goetz et al., 2015; Johnson et al., 2000; Swanston, 1969). Extreme wind gusts have also been implicated in landslide initiation (Buma and Johnson, 2015; Lin et al., 2025; Parra et al., 2021) although the relative importance is difficult to determine and the mechanism by which wind gusts may contribute to slope failure is unclear and may include physical disturbance, progressive root failure, directed rainfall, or opening of hydrological pathways (Guthrie et al., 2010; Rulli et al., 2007).

The runout and inundation of landslides in post-glacial settings tends to be highly variable owing to variations in landscape dissection and the availability of unconsolidated material for entrainment. Most generally, the weakly-dissected slopes tend to generate fewer mobile slides that deposit on steeper slopes compared to slides in unglaciated settings (Booth et al., 2023; Vascik et al., 2021). Forest cover also affects landslide mobility, and the dense forest cover and large woody debris characteristic of many post-glacial settings favour lower mobility landslides (Booth et al., 2020). An abundance of datasets and models for the production and redistribution of colluvium that contribute to debris flow entrainment and volumetric growth have been generated in unglaciated settings (DiBiase et al., 2017; Gorr et al., 2022; Guilinger et al., 2023; Lamb et al., 2011; Reid et al., 2016; Rengers et al., 2020), but we lack both a framework and datasets that enable us to predict the runout, volume, and inundation of debris flows in post-glacial settings.

The need to improve our understanding of post-glacial shallow landslide triggers and processes in SE Alaska was highlighted by a large, catastrophic landslide that occurred on Wrangell Island on the evening of November 20, 2023. The landslide initiated during an intense rainfall event and entrained large quantities of colluvium and trees as it travelled downslope (Fig.1). Before terminating in Zimovia Strait, the landslide travelled over 1 km, inundated Zimovia Highway, destroyed three homes, and caused six fatalities (Nicolazzo et al., 2024), making it one of the deadliest landslides in Alaska history. This event was preceded and followed by several other fatal landslides in the region, including the 2015 Sitka, 2020 Haines, and 2024 Ketchikan events. This concentration of activity motivates a detailed assessment of the geomorphic, geologic, and atmospheric factors contributing to the initiation and runout of impactful landslides in SE Alaska. Here, we use an array of tools to characterize the 2023 Wrangell landslide and describe how these findings will advance our ability to assess landslides in the region. In particular, our analysis addresses: 1) atmospheric processes, including precipitation and wind, that contributed to event triggering, 2) controls on the accumulation of unconsolidated material that promotes landslide initiation, downslope entrainment, and volumetric growth, 3) geologic and topographic controls on landslide runout and inundation, and 4) controls on the organization and evolution of upslope drainage networks that modulate hydrologic response at the initiation zone. We leverage field observations, geotechnical measurements, sample analyses, climate data, change detection analysis from

https://doi.org/10.5194/egusphere-2025-4123
Preprint. Discussion started: 9 September 2025

96 sequential airborne lidar data, an existing US Forest Service landslide inventory, and hydrologic flow routing analyses to assess
97 the 2023 Wrangell landslide. Our findings provide critical information for identifying landslide triggers, mapping susceptible
98 initiation zones, and modelling runout and inundation, and we propose specific steps and research needs to advance landslide
99 assessment in SE Alaska and other post-glacial landscapes to help reduce risk and minimize exposure during future events.

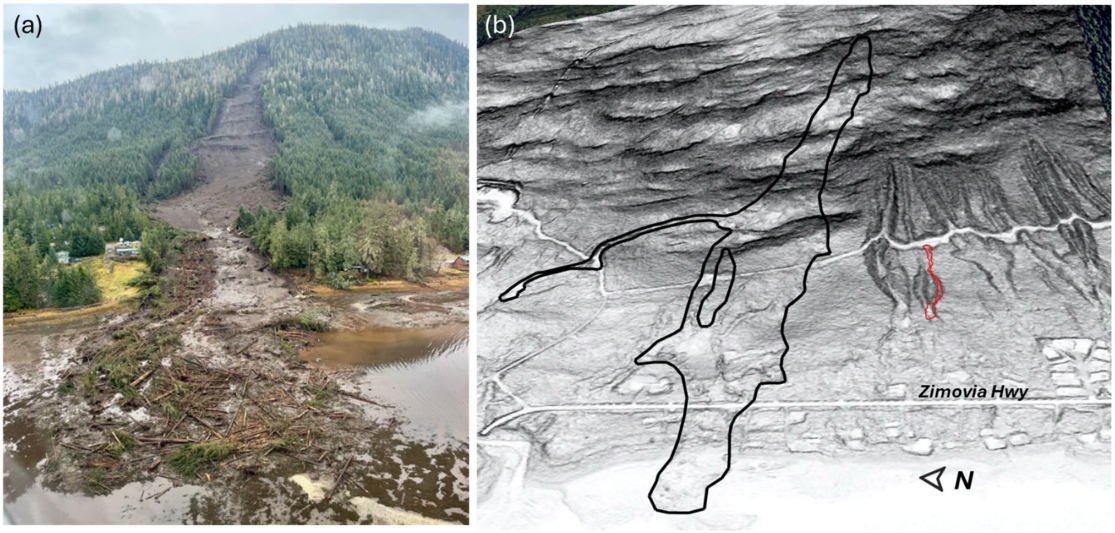

100 **Figure 1.** The November 20, 2023 MP11.2 Wrangell landslide: **(a)** Oblique aerial photograph facing east taken on November 22, 2023 by
101 B. Salisbury (DGGS), and **(b)** oblique lidar slopeshade image.

102 **2 Study site**

103 **2.1 Geology and geomorphology**

104 Situated in the southern half of southeast (SE) Alaska, Wrangell Island (Fig. 2) is composed of an assemblage of marine rocks
105 in the Gravina coastal belt on the eastern margin of the Alexander Terrane that composes a substantial fraction of the region
106 (Fig. 2b) (Haeussler, 1992; Wheeler and McFeely, 1991). Bedrock of the northern half of the island includes Cretaceous and
107 Jurassic graywacke and Cretaceous intrusions (Karl et al., 1999). These turbidites and igneous rocks were deformed in the
108 Late Cretaceous during the closing of a marine sedimentary basin between the Alexander terrane to the west and the Stikine
109 terrane to the east (Haeussler, 1992). The graywacke is part of the Seymour Canal Formation, a unit with fine-grained,
110 rhythmically bedded turbidite deposits that are regionally recrystallized to slate or phyllite. The sandstone layers tend to be
111 highly resistant and often form bedrock cliffs in areas with favorable dip direction.

112

https://doi.org/10.5194/egusphere-2025-4123
Preprint. Discussion started: 9 September 2025

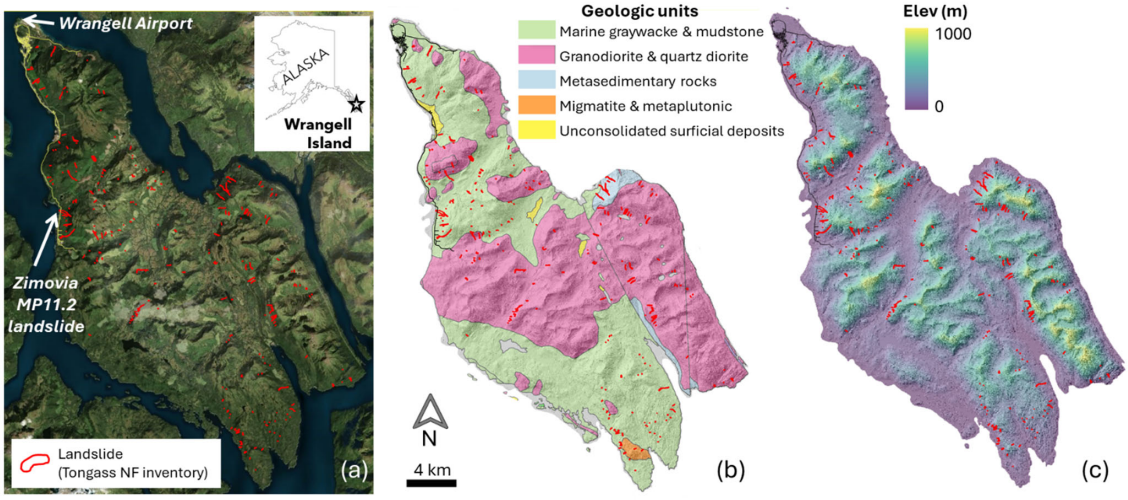

113 **Figure 2**. Maps of Wrangell Island overlain with 256 landslide polygons (red) from the Tongass National Forest Landslide
114 Inventory (TNFLI): (**a**) satellite imagery from Bing Satellite layer in QGIS Quick Map Services plug-in, (**b**) geologic units,
115 and (**c**) lidar elevation and hillshade image.

116 The SE Alaska archipelago, including Wrangell Island, has been repeatedly glaciated, most recently during the Last Glacial
117 Maximum, generating characteristic landforms, including cirques, uplifted shorelines, and broad U-shaped valleys (Fig. 2c)
118 (Hamilton, 1994; Mann and Hamilton, 1995). By 13 to 15 kya, the margins of the Cordilleran Ice Sheet had retreated from SE
119 Alaska fjords, channels, and interior passages, leaving isolated or stranded ice caps on some islands, with alpine or tidewater
120 glaciers in many valleys and mountain peaks protruding above alpine glaciers (Carrara et al., 2003; Menounos et al., 2017).
121 Broad and gentle uplifted shorelines (sometimes more than 100 m above sea level) with beach ridges, storm berms, and weak
122 dissection, are abundant along coastlines in portions of SE Alaska (Baichtal et al., 2021) and may influence landslide runout.
123 On hillslopes, post-glacial landscape evolution is highly variable and some areas, particularly portions of western Wrangell
124 Island, experience widespread slope modification from rockfall, talus accumulation, localized gullying, and landsliding.

125 **2.2 Climate and vegetation**

126 SE Alaska is a regional temperate rain forest with a maritime climate (Wendler et al., 2016). In Wrangell the mean annual
127 precipitation is roughly 2 m, most of which falls as rain at low elevation with the proportion of rain-to-snow decreasing with
128 elevation. In Wrangell and across SE Alaska, nearly all high-intensity rainstorms are associated with atmospheric rivers (ARs)
129 (Nash et al., 2024), which are long (>2000 km), narrow (<500 km), moisture-laden currents in the lower troposphere (Neiman
130 et al., 2008; Ralph et al., 2004). When ARs, which are most active August to November in SE Alaska, make landfall, orographic
131 forcing can result in higher precipitation in mid-slope locations and on slope aspects that coincide with the trajectory of

https://doi.org/10.5194/egusphere-2025-4123
Preprint. Discussion started: 9 September 2025

incoming ARs (Marra et al., 2022; Rulli et al., 2007). Although ARs account for only ~33% of annual precipitation, they generate 90% of extreme precipitation in the region (Sharma and Déry, 2020). As a result, ARs trigger the vast majority of shallow landslides along the Pacific coast of North America and SE Alaska (Cordeira et al., 2019; Oakley et al., 2018)

Much of SE Alaska is densely forested with mixed conifer forests of western hemlock (*Tsuga heterophylla*), Sitka spruce (*Picea sitchensis*), western red cedar (*Thuja plicata*), yellow cedar (*Callitropsis nootkatensis*), and mountain hemlock (*Tsuga mertensiana*) (Harris and Farr, 1974; Hees and Mead, 2005). Disturbed and riparian areas host locally abundant red alder and black cottonwood. Non-forested regions include high-elevation tundra vegetation and emergent wetlands (e.g., muskeg), surface water, glaciers, and snow/icefields (Flagstad et al., 2018). On Wrangell Island, logging since the 1950's along lower elevations has resulted in a mosaic of forest stand age. Although recent hemlock sawfly and western blackheaded budworm outbreaks have resulted in swaths of mid-elevation trees that have dropped their needles (Howe et al., 2024), the extent of tree mortality and impact on root systems, and thus slope stability, is not yet established.

2.3 Landslides in Southeast Alaska

Based on the Tongass National Forest Landslide Inventory (TNFLI), which includes >20,000 mapped slope failures and slide-prone areas (U.S. Forest Service, 2025b), the vast majority (>80%) of landslides in SE Alaska are debris flows or unchannelized debris avalanches that initiate within weathered till or colluvium during periods of intense rainfall (Fig 2a). The recent fatal landslides in SE Alaska were colluvial landslides, except for the 2020 Beach Road landslide in Haines that initiated within shallow bedrock during the December 2020 rain-on-snow event (Darrow et al., 2022). Extensive field-based research on landslide processes, particularly root reinforcement and hydrologic response, originated in the 1960s on Prince of Wales Island following increased landslide activity after timber harvest (Johnson et al., 2000; Swanston, 1969, 1970, 1973). These studies indicated that tree mortality affected landslide density as well as runout, such that landslides in harvested areas exhibited higher mobility (Booth et al., 2020; Buma and Johnson, 2015). The wide glacial valleys and weakly-dissected slopes in SE Alaska tend to favour infrequent landslide delivery to streams and most debris flow deposits contribute to fans or footslope deposits.

2.4 The November 20, 2023 atmospheric river and impacts on Wrangell Island

A hurricane-force 964 mb low pressure system lifted out of the North Pacific into the Gulf of Alaska during the early morning hours of November 20, 2023 (Figure 3a). This low-pressure system proceeded along a north-northwest track, with the warm front moving over southern and central SE Alaska before the front pushed north through the evening hours (Fig. 3b). A cold air mass over northern SE Alaska and the Yukon produced a zone of high pressure and a strong pressure gradient across SE Alaska. This colder air likely produced some snowfall at higher elevations prior to the arrival of warm, moist air. This weather system included significant subtropical moisture and additional AR characteristics evident in satellite imagery (Fig. 3c). At 3 PM on November 20, the CIMMS Model analysis of Integrated Water Vapor Transport (IVT), a commonly used indicator of ARs, indicated very high IVT over the southern half of SE Alaska (Fig. 3d).

https://doi.org/10.5194/egusphere-2025-4123
Preprint. Discussion started: 9 September 2025

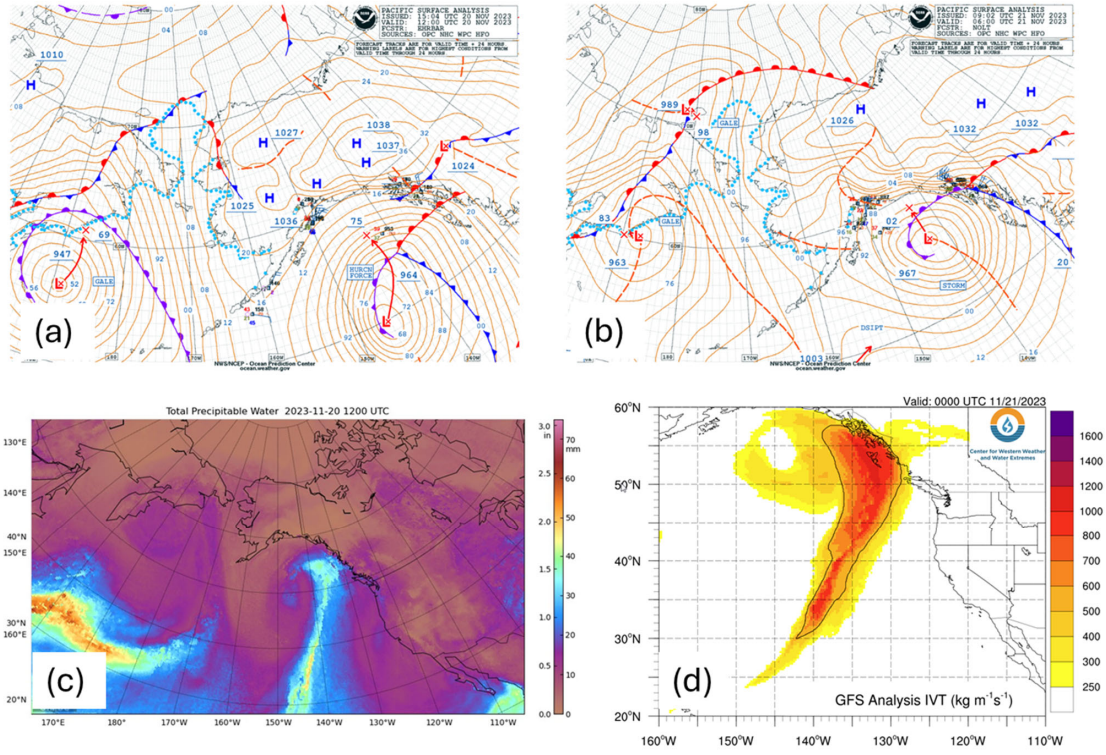

Figure 3. The November 20, 2023 atmospheric river event: (**a**) NOAA surface analysis from imagery from November 20 at 4am Alaska Standard Time, (**b**) NOAA surface analysis from imagery from November 20 at 10pm Alaska Standard Time, (**c**) Total Precipitable Water from the Cooperative Institute for Meteorological Satellite Studies (CIMSS) Morphed Integrated Microwave Total Precipitable Water (MIMIC-TPW) for November 20 at 4am Alaska Standard Time, (**d**) Integrated Water Vapor Transport (IVT) from Center for Western Weather and Water Extremes (C3WE) from November 20 at 4pm.

Heavy precipitation and high wind gusts began in the morning hours of November 20 and warm air and moisture likely melted snow at higher elevations. That afternoon, numerous landslides and road blockages were reported on Prince of Wales Island near Craig, Klawock, and Black Bear. The front shifted to an eastward trajectory in the early evening hours, as heavy rain and winds shifted towards Wrangell Island, and reports of the Zimovia Highway mile point (MP) 11.2 landslide were received just before 9 pm Alaska Standard Time. The front continued eastward, and rain and winds diminished through the night. The 24-hr precipitation totals on Prince of Wales varied from <5m to >16 cm on the east and west sides of the island, respectively (National Oceanographic and Atmospheric Administration (NOAA), 2024). At Wrangell airport, which is situated at sea level near the northern tip of the island and over 15 km north of the MP11.2 landslide (Fig. 2a), 8 cm of rainfall was recorded in 24

https://doi.org/10.5194/egusphere-2025-4123
Preprint. Discussion started: 9 September 2025

hours, and nearly half of that rainfall total was delivered steadily between 3 pm and 9 pm (Fig. 4). Peak wind speed and gusts of 30 and 50 km hr-1, respectively, occurred from 11 am to 3 pm and sustained at high levels through the evening. Air temperature rose rapidly in the morning and remained above 5°C. A remote weather station located ~25 km west of the MP11.2 slide at 275m above sea level on Zarembo Island recorded similar wind speeds as the Wrangell airport but notably logged a short period of gusts >100 km hr-1 around 7 pm in conjunction with a southward shift in direction of the front (Nicolazzo et al., 2024). Local observations during the day of the storm are notable because several residents reported: 1) rainfall to be more intense along Zimovia Highway than in Wrangell, and 2) significant snow cover at mid-to-high elevations prior to the November 20 storm that melted by November 21.

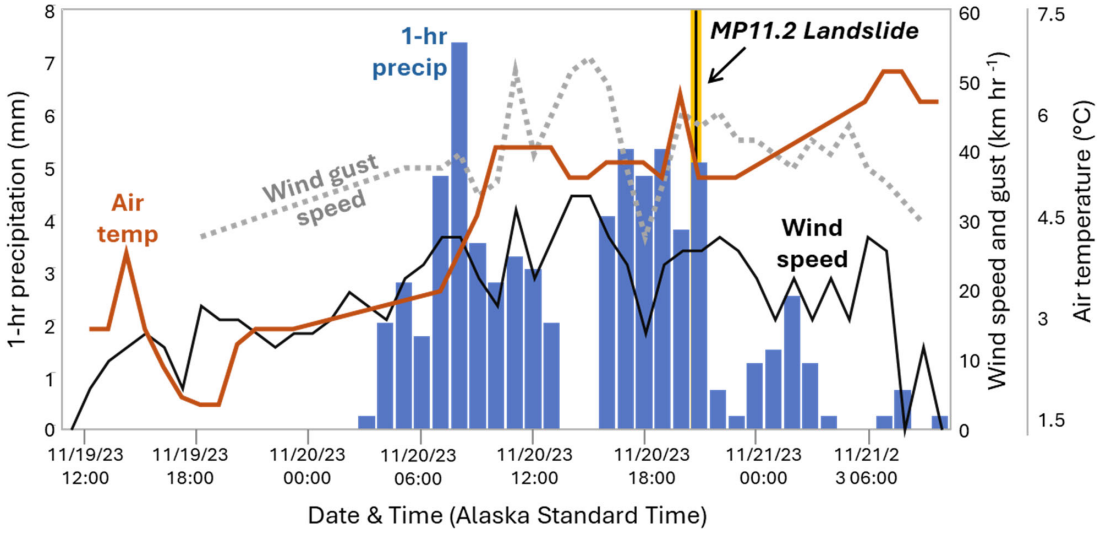

Figure 4. Time series of hourly climate data from Wrangell Airport spanning November 19 to 21, 2023, including: 1-hr precipitation (blue bars), average wind speed and maximum wind gusts (black and dashed grey lines, respectively), and air temperature (red line). The MP11.2 landslide occurred at ~9pm on November 20 (vertical yellow/black line).

On November 21, Alaska Governor Dunleavy issued a state disaster declaration, and the Alaska Division of Geological & Geophysical Surveys (DGGS) was contracted to document landslides triggered on Wrangell Island during the storm. DGGS used airborne lidar acquired in July and on November 28-29, 2023, to estimate the character and volume of the MP11.2 and nearby landslides (Nicolazzo et al., 2024). For the MP11.2 landslide, they noted under 80,000 m3 of erosion, thick soil entrained along bedrock benches, and an abundance of soil and large woody debris (with a negligible amount of bedrock) composing the deposit. Portions of the deposit had been removed before the post-event lidar acquisition and the deposit

https://doi.org/10.5194/egusphere-2025-4123
Preprint. Discussion started: 9 September 2025

travelled nearly 150 m into the ocean, such that a small but non-negligible fraction of the deposit was not captured with lidar differencing.

3 Methods

3.1 Overview

To assess and quantify controls on the initiation and runout of the MP11.2 landslide, we performed a wide array of analyses and generated observations from fieldwork, community events, airborne lidar, hydrologic modelling, weather data, and geotechnical testing. We endeavoured to address community-generated queries, such as the potential role of wind as a triggering agent and mechanisms responsible for the anomalously large size of the landslide.

3.2 Landslide geometry

To contextualize the MP11.2 landslide, we analysed the landslides previously mapped on Wrangell Island included in the TNFLI (n=20,235) (U.S. Forest Service, 2025b). We excluded snow avalanche chutes, snow avalanche fields, and debris avalanche fields because these extensive features reflect landforms that accumulate over time rather than discrete landslide events. For the remaining landslides (n=14,670), we identified those occurring on Wrangell Island and quantified the area, mobility (defined as H/L, where H is elevation difference between the head scarp and deposit and L is landslide length, defined as the horizontal distance between the head scarp and deposit), and aspect ratio (defined as W/L, where W is average landslide width).

3.3 Field observations, sampling, and analyses

To document failure mechanisms and runout behaviour, we traversed the entire length of the landslide, observing evidence of entrainment and deposition, and mapping localized seepage in the head scarp area. We collected representative soil samples, from which we determined gravimetric water content (American Society for Testing Materials, 2017a); particle-size distribution, consisting of sieve analysis (American Society for Testing Materials, 2017b), sedimentation analysis (American Society for Testing Materials, 2021), and specific gravity testing (American Society for Testing Materials, 2014b); Atterberg limits (American Society for Testing Materials, 2017a), and organic content by loss on ignition (Alaska Department of Transportation and Public Facilities, 2023). We also collected two volumetric samples using a soil sampler with inner brass rings, from which we determined dry unit weight and volumetric water content. We classified samples using the Unified Soil Classification System (American Society for Testing Materials, 2017a). We also collected estimates of intact bedrock strength using two Rock Schmidt Rebound Hammers (N-type and L-type, with impact energies of 2.207 Nm and 0.735 Nm, respectively). We followed standard methods (American Society for Testing Materials, 2014a) with the exception that we did not use a grinding stone on the in-situ rock faces. We also collected slices (or “cookies”) of four trees entrained in the deposit to determine their ages and obtained 35 bedrock and/or joint surface orientation measurements for kinematic analysis. Finally,

https://doi.org/10.5194/egusphere-2025-4123
Preprint. Discussion started: 9 September 2025

we ventured onto the ridgetop above the landslide to document the upslope accumulation area that contributes surface water flow to the head scarp region.

3.4 Topographic analysis: change detection, morphology, and hydrologic modelling

To quantify the pattern of erosion and deposition, and controls on colluvial deposits and their entrainment in the landslide, we used the July 2023 and November 2023 lidar for change detection and topographic analysis. Both datasets have 0.5-m pixel spacing, high bare earth point density (>5 pts m^{-2}), and high accuracy (<10 cm error in bare and vegetated areas). We used QGIS for our analyses and mapped the landslide extent using high-resolution imagery acquired by the Alaska Department of Transportation and Public Facilities (ADOT&PF) and the airborne lidar data. By comparing numerous stable features in both lidar datasets we determined systematic offset to be negligible (<5cm). For change detection, we applied raster-based subtractions and created a point layer for the landslide pixels, which we attributed with slope, elevation, land surface change using the digital terrain model (DTM, i.e., bare earth data), and vegetation change using the digital surface model (DSM,i.e., first return data). We used the derived points and their attributes in three primary ways: 1) maps of DTM and DSM change across the landslide and surrounding terrain, 2) plots of swath (10-m wide) averaged profiles of elevation, slope, and DTM / DSM change along a longitudinal transect that spans the central axis of the primary landslide, and 3) construction of a comprehensive mass balance of DTM change (i.e., erosion and deposition) along a cross-sectional transect that spans the entire width of the landslide.

For the hydrologic modelling, we used TopoToolbox to define flow paths above the landslide scarp by removing sinks and defining flow directions and flow accumulation using a multiple flow direction (MFD) algorithm that partitions flow to all downslope pixels in proportion to the gradient of each pixel (Schwanghart and Scherler, 2014). In addition, we accessed the U.S. National Wetlands Inventory (Flagstad et al., 2018) in conjunction with our flow model to assess the potential contribution of wetlands to surface water flow and landslide triggering.

4 Results

4.1 Landslide geometry

The MP11.2 landslide has an area greater than 142,000 m2 and initiated at 454m above sea level before flowing downslope >1km and depositing into the coastal marine environment (Fig. 5a). Although the width of the landslide averages 130 m, it is widest in the middle of the runout zone, and relatively narrow (<50m) at the initiation zone and terminus. Our analysis of landslides on Wrangell Island and in the TNFLI demonstrates that the MP11.2 landslide is notable for its areal extent (Fig. 6a), which is more than twice the size of the next largest Wrangell Island landslide. When compared to the entire TNFLI, the MP11.2 landslide has a larger area than 99.5% of the landslides (Fig. 6b), which further demonstrates its exceptional size.

Given that landslide mobility (quantified as H/L, the value of which decreases with increased mobility) tends to vary with landslide size (Iverson et al., 2015; Rickenmann, 1999), we plotted H/L versus landslide area for the Wrangell Island landslides

https://doi.org/10.5194/egusphere-2025-4123
Preprint. Discussion started: 9 September 2025

and fitted a logarithmic trend, such that H/L decreases slightly with area (Fig. 7a). In this context, the MP11.2 landslide is situated on the trend and thus does not appear notable for its mobility relative to its area. Because the MP11.2 landslide maintained a relatively wide footprint along most of its path, we also plotted W/L versus area (Fig. 7b) and noted a robust power-law trend indicating that slides tend to become increasingly elongate as they get bigger. In this context, the MP11.2 landslide is anomalous for its large W/L value relative to its area. Specifically, the landslide plots well above the trend and only one of the 25 next largest landslides has a similar positive deviation above the area-W/L curve (Fig. 7b). In summary, the landslide did not appear to exhibit uncommon mobility as defined by H/L values, but rather it attained a large area while also maintaining substantial width, which contributed to its extensive inundation area and devastating impact.

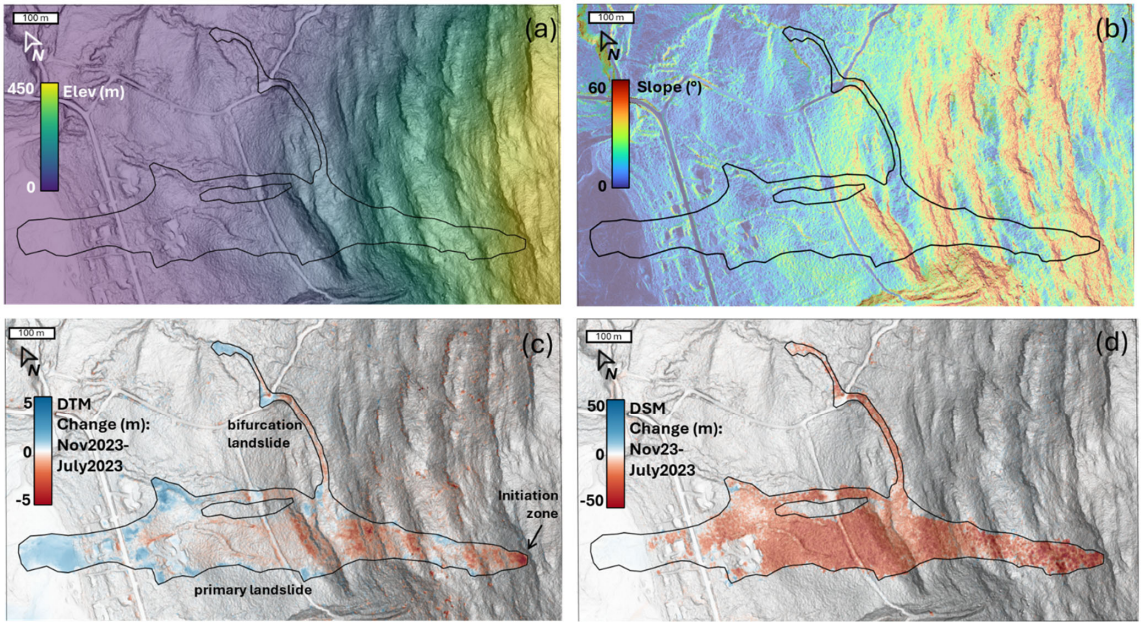

Figure 5. Lidar-derived maps of the MP11.2 landslide: (**a**) elevation above sea level in meters, (**b**) slope in degrees, (**c**) DTM change (land surface or bare earth), and (**d**) DSM change (first return or canopy) with November 2023 dataset subtracted from the July 2023 dataset such that negative values (red) reflect decreases and positive values (blue) reflect increases.

https://doi.org/10.5194/egusphere-2025-4123
Preprint. Discussion started: 9 September 2025

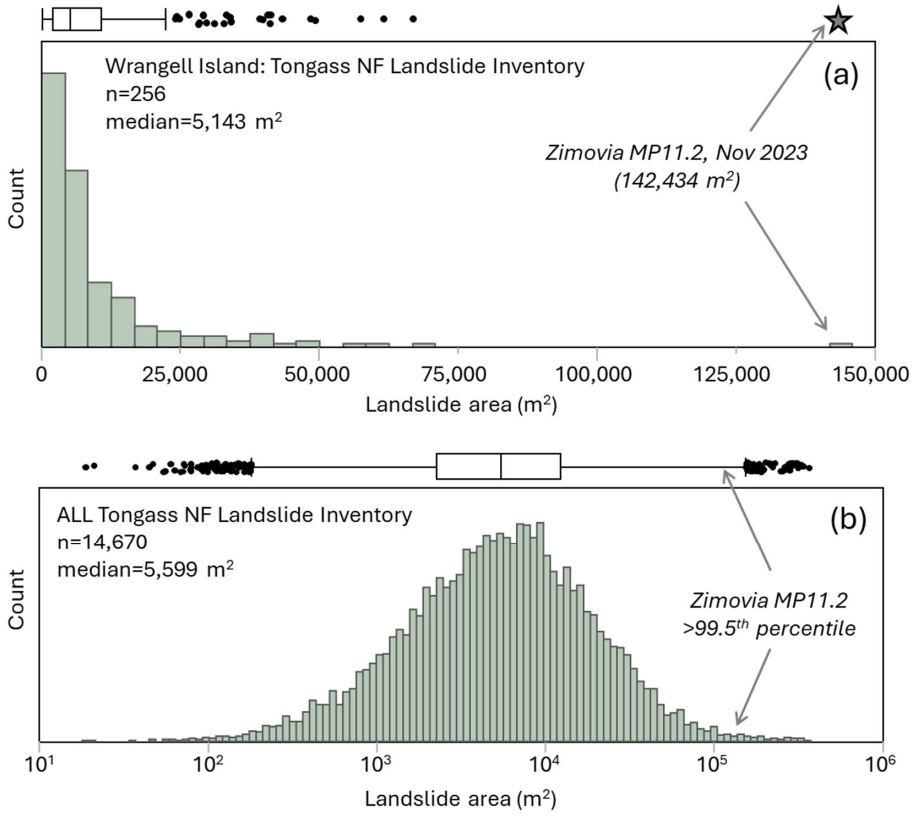

268 **Figure 6.** Histograms of landslide area from the TNFLI for (**a**) Wrangell Island and (**b**) all of TNLFI, note the log scale. The
269 box-whisker plots above each histogram convey the median, interquartile range and outliers and the star denotes the MP11.2
270 landslide.

https://doi.org/10.5194/egusphere-2025-4123
Preprint. Discussion started: 9 September 2025

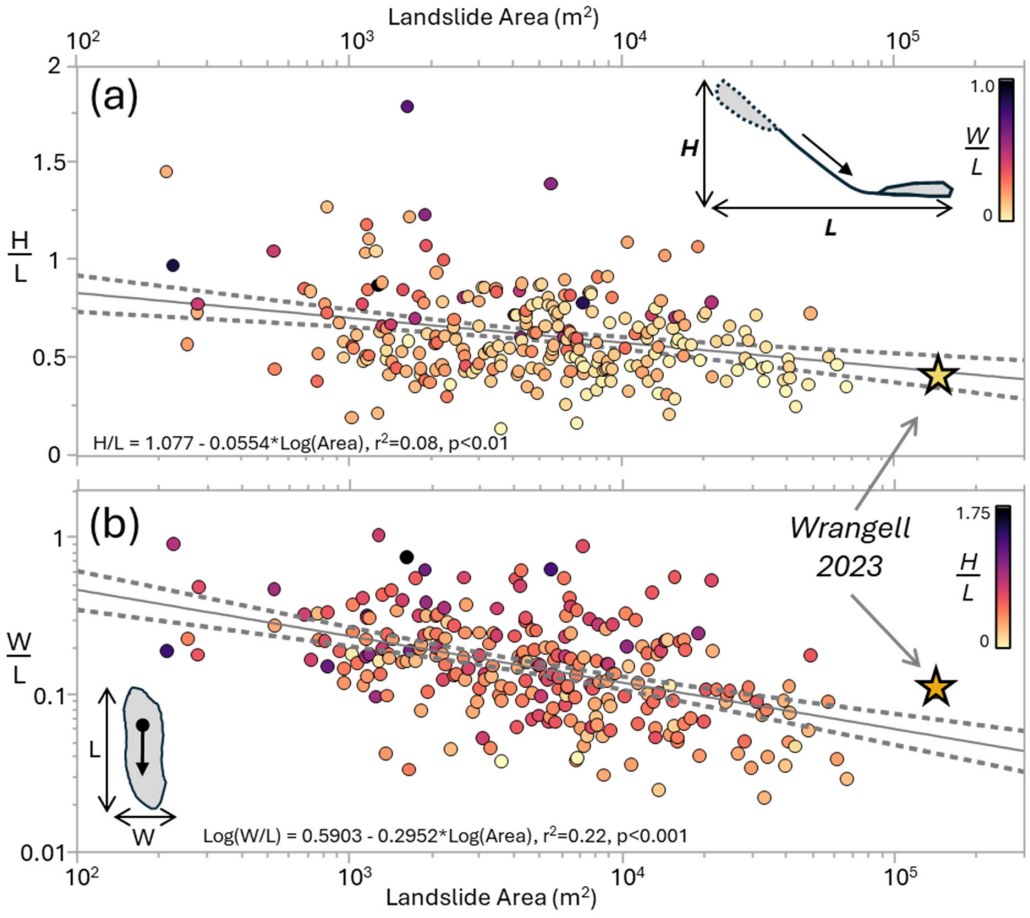

271 **Figure 7**. Plots of landslide characteristics for Wrangell landslides in the TNFLI. (**a**) Variation of mobility (H/L) with area,
272 and (**b**) variation of landslide aspect ratio with area. Note that the star indicates the MP 11.2 landslide in a and b. The solid
273 black and dashed grey lines denote the regression fits and 95% confidence intervals for the equations indicated in a and b.
274 Individual points are coloured by W/L in a and H/L in b.

275 **4.2 Geologic units, bedrock structure, and soil properties**

276 Marine sedimentary rocks of the Seymour Canal Formation (Karl et al., 1999) are exposed in the landslide and a bedrock
277 quarry approximately 1.5 km north of the landslide head scarp (NE corner of map in Fig. 8). Bedrock lithology includes
278 interbedded shale and graywacke typical of turbidite sequences with bedding dipping into the hillslope (to the east) within the
279 landslide (Fig. 8). Local metasedimentary rocks on nearby hillslopes (slate and minor phyllite) indicate low-grade

https://doi.org/10.5194/egusphere-2025-4123
Preprint. Discussion started: 9 September 2025

metamorphism in the study area. Graywacke beds are 0.25- to 5-m thick as observed in the field and form benchlike topography, with the resistant graywacke creating subvertical cliff bands within the landslide margin and across undisturbed hillslopes, and the relatively weak shale forming low-gradient slopes (Fig. 5b). Bedding orientation in the quarry dips to the southeast, indicating hillslope-scale folding (Fig. 8). In addition to bedding geometry, we documented three joint sets to assess the potential for rock slope instability along the resistant bedrock cliffs. Preliminary kinematic analysis of discontinuities using conservative friction angle estimates of 15° and 30° for shale and sandstone, respectively (Gonzalez de Vallejo and Ferrer, 2011), indicates that flexural toppling is possible while other rock failure mechanisms (direct toppling, wedge and planar failure) are unlikely (supplemental materials).

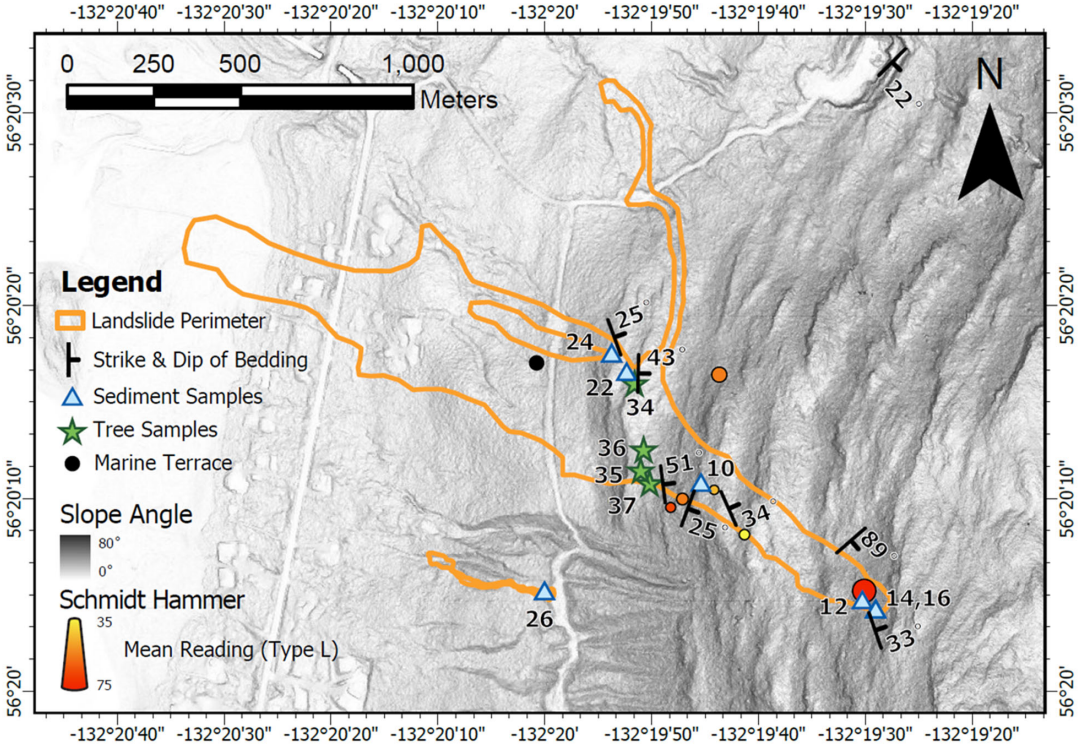

Figure 8. Lidar hillshade map of MP11.2 landslide showing locations of field measurements and samples acquired during the August 2024 field campaign. Strike and dip and Schmidt Hammer values denote averages within each sample locale.

We collected a total of 60 readings with each of the Schmidt Hammers. Using a correlation for sandstone, siltstone, and mudstone that does not require rock density and uses the L-type hammer (Aydin and Basu, 2005), our estimates of uniaxial

https://doi.org/10.5194/egusphere-2025-4123
Preprint. Discussion started: 9 September 2025

compressive strength (UCS) average 90 MPa for measurements taken outside the lateral margins of the landslide body, 82 MPa for measurements in the middle of the landslide body, and 148 MPa for measurements taken on massive greywacke exposed in the head scarp (supplemental materials). These values are typical for graywacke (Gonzalez de Vallejo and Ferrer, 2011) and indicate that the estimated UCS of the exposed graywacke in the head scarp is 80% higher than that within the lower landslide body and 64% higher than bedrock exposures adjacent to the MP11.2 landslide.

In exposures along the landslide flanks, we observed colluvium as discontinuous "wedges" at the base of bedrock cliffs, including a ~4 m thick deposit that constitutes the initiation zone (Fig. 9a). The matrix of the colluvium was brown, organic silty sand to silty sand with gravel (SM), similar to displaced landslide material observed downslope. The material properties of the colluvium imply moderate frictional strength, minimal weathering or alteration, and relatively high permeability. All of the samples tested were non-plastic (supplementary materials). In an area scoured by the landslide in its depositional zone, we also observed a deposit of sand and subrounded, imbricated gravel characteristic of coastal marine sediments. The deposit is exposed just below the USFS road at approximately 100 m elevation, which is consistent with estimated glacial isostatic adjustment documented for the region (Baichtal et al., 2021).

https://doi.org/10.5194/egusphere-2025-4123
Preprint. Discussion started: 9 September 2025

Figure 9. Photographs of key features identified in the field: (**a**) view to the north across the head scarp, exposing thick (~4m) colluvial wedge in lateral margin, (**b**) ridgetop wetland or muskeg that drains to the head scarp, and (**c**) oblique view of mid-slope location (~1000m on transect; see Fig. 11) depicting high relief and resistant cliff-forming unit and patch of live blueberry bushes just below the top of the bedrock cliff. Note person for scale.

4.3 Landslide initiation and triggering factors

The initiation zone for the MP11.2 landslide has an average slope of 42±2.5° and is approximately 30-m wide and 26-m long (Fig. 5b, d). According to lidar differencing of the pre- and post-event DTMs, the average thickness of the initiation zone is 4.5±0.7 m (Fig. 5c), which is thick relative to many landslides observed in the Tongass National Forest. In the days following the landslide, aerial imagery acquired by the Alaska Department of Transportation and Public Facilities (ADOT&PF) revealed prodigious seepage emanating from the SE corner of the head scarp, and during our August 2024 field campaign we noted localized seepage in that location despite negligible rainfall in the preceding days. Additional triggering factors include

https://doi.org/10.5194/egusphere-2025-4123
Preprint. Discussion started: 9 September 2025

compromised root reinforcement, and we noted an abundance of standing Western hemlock trees without needles just beyond the northern and southern margins of the initiation zone.

In the 6 hours prior to the MP11.2 landslide, rainfall intensity at the airport averaged 5 mm hr-1 (Fig. 4), which corresponds to a ~1-yr return interval (National Oceanographic and Atmospheric Administration (NOAA), 2024). In addition, the maximum 3-hr intensity just prior to the slope failure was less than the 7 mm hr-1 intensity threshold that delineates an elevated level of risk in the Sitka region. Notably, high winds and warm temperatures characterized the 12-hour period prior to the landslide, and these changes may have contributed to the failure through mechanical disturbance and rapid delivery of snowmelt to the initiation zone, respectively. Observational records of these potential triggering factors are lacking, so we explored alternative sources of evidence. To assess the potential role of wind disturbance in landslide triggering we used differencing of the canopy (or DSM) lidar data to map wind throw (or tree turnover) as a signature of canopy disturbance proximal to the initiation zone (Fig. 5d). Consistent with our field observations, our map of DSM change does not reveal evidence for widespread canopy disturbance beyond the margins of the landslide. In fact, the DSM change map revealed less than 10 individual and localized tree turnover events dispersed within several kilometres of the MP11.2 landslide.

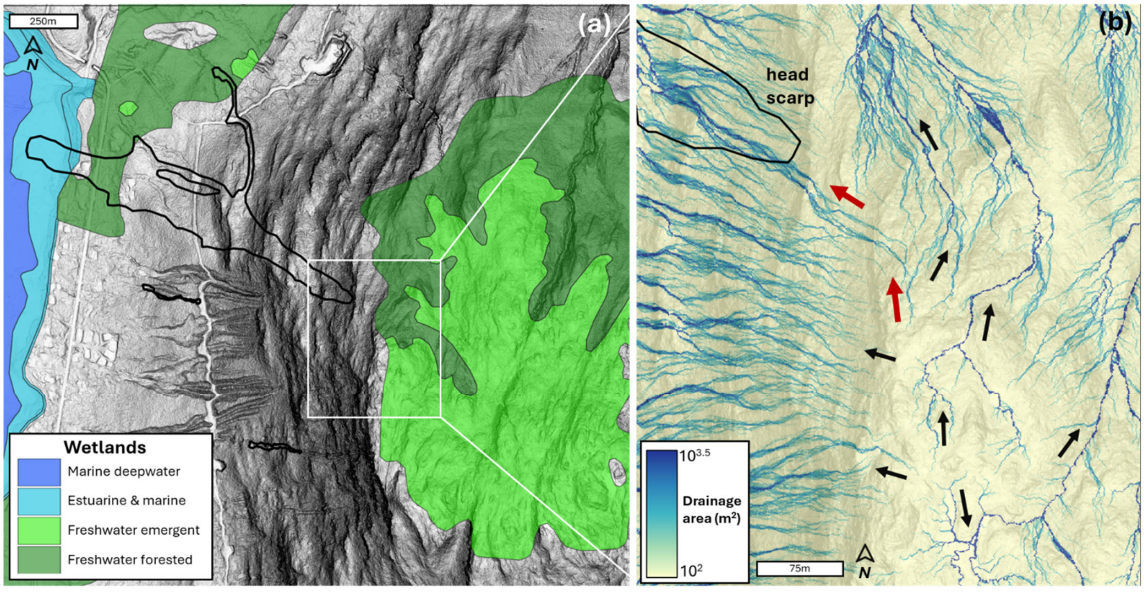

Figure 10. Lidar maps of MP11.2 landslide and relevant drainage features. (**a**) Shaded relief image of landslide and extent of ridgetop wetland from the National Wetlands Inventory, (**b**) map of contributing drainage area along the ridgetop above the MP11.2 landslide. Note the radial flow pattern that includes a significant area flowing to the head scarp (red arrows).

https://doi.org/10.5194/egusphere-2025-4123
Preprint. Discussion started: 9 September 2025

To assess the potential contribution from ridgetop wetlands and rapid snowmelt on the saturation of the initiation zone, we mapped wetlands and hydrological flow paths upslope of the head scarp (Fig. 10a). Our map shows a radial drainage pattern emanating from the ridgetop with an array of dispersed, west-directed flowpaths that drain to slide-prone slopes to the south of the MP11.2 landslide (Fig. 10b). By contrast, flowpaths oriented to the north, east, and south tend to exhibit an incised and well-defined channel network structure that is reflected by the narrow, dark blue (high drainage area) tendrils that contrast with the more diffusive flowpaths with wider and lighter blue (lower drainage area) signatures draining west (Fig. 10b). This pattern likely reflects the relative antiquity of channels and flowpaths draining from the ridgetop to the north, east, and south. Notably, an elongate system of flowpaths is situated between the west- and north-directed drainages. This flow accumulation pathway denoted by red arrows in Fig. 10b demarcates a substantial drainage area directed to the SE corner of the MP11.2 landslide head scarp and coincident with abundant seepage observed in the field. Our flow mapping indicates greater than 6,000 m2 of drainage area upslope of the head scarp, and this source area includes a substantial fraction of low-gradient, emergent wetlands with patchy bedrock exposure (Fig. 9b, 10a). In the field, this ridgetop wetland area (muskeg) was characterized by deep (>2m), organic soil akin to peatlands. Curiously, the flowpaths that contribute to the landslide head scarp also reveal evidence of bifurcation into slide- and north-directed drainage systems (Fig. 10b). Our field observations indicate that this bifurcation corresponds to meter-scale roughness in the bedrock/wetland surface, implying that the orientation of ridgetop drainage may be highly dynamic and sensitive to local disturbances.

4.4 Landslide runout and mass balance

Our lidar and field analyses reveal strong topographic and geologic controls on the pattern of erosion and deposition along the landslide runout path (Fig. 11). These analyses focus on the primary landslide path and do not include the north-directed bifurcation that occurred in the middle sections and accounted for a small fraction of the slide volume. Our field observations indicate that the initiation zone was localized to the upper 30 m (~1350 m on our transect; Fig. 11a) such that runout processes are responsible for the downslope pattern of erosion and deposition. The W-NW directed path of the slide does not exhibit topographic convergence as expressed by contour (or planform) curvature and thus lateral confinement did not affect the runout behaviour. Rather, our 10-m wide swath-averaged transect data show that the lower half of the ~1,250-m long runout is characterized by a low-gradient surface with slope angles that seldom exceed 20° (Fig. 11a-c). This zone of relatively gentle topography coincides with our observations of nearshore/coastal deposits found at approximately 100 m above sea level. In contrast, the upper half of the runout zone (between 800 and 1300 m along our transect) is characterized by a sequence of 5 to 7 step-bench segments (Fig. 11c). Steep cliffs of exposed bedrock are defined by east-dipping resistant graywacke beds that manifest as continuous ledges across the landscape (Fig. 1). The intervening low-gradient (<20°) benches tend to be broad and approximate bedding planes with a carapace of locally derived colluvium. These steps composed of cliff-bench sequences are ubiquitous in the marine sedimentary units across Wrangell Island and they are associated with numerous long-runout landslides in the TNFLI.

https://doi.org/10.5194/egusphere-2025-4123
Preprint. Discussion started: 9 September 2025

370

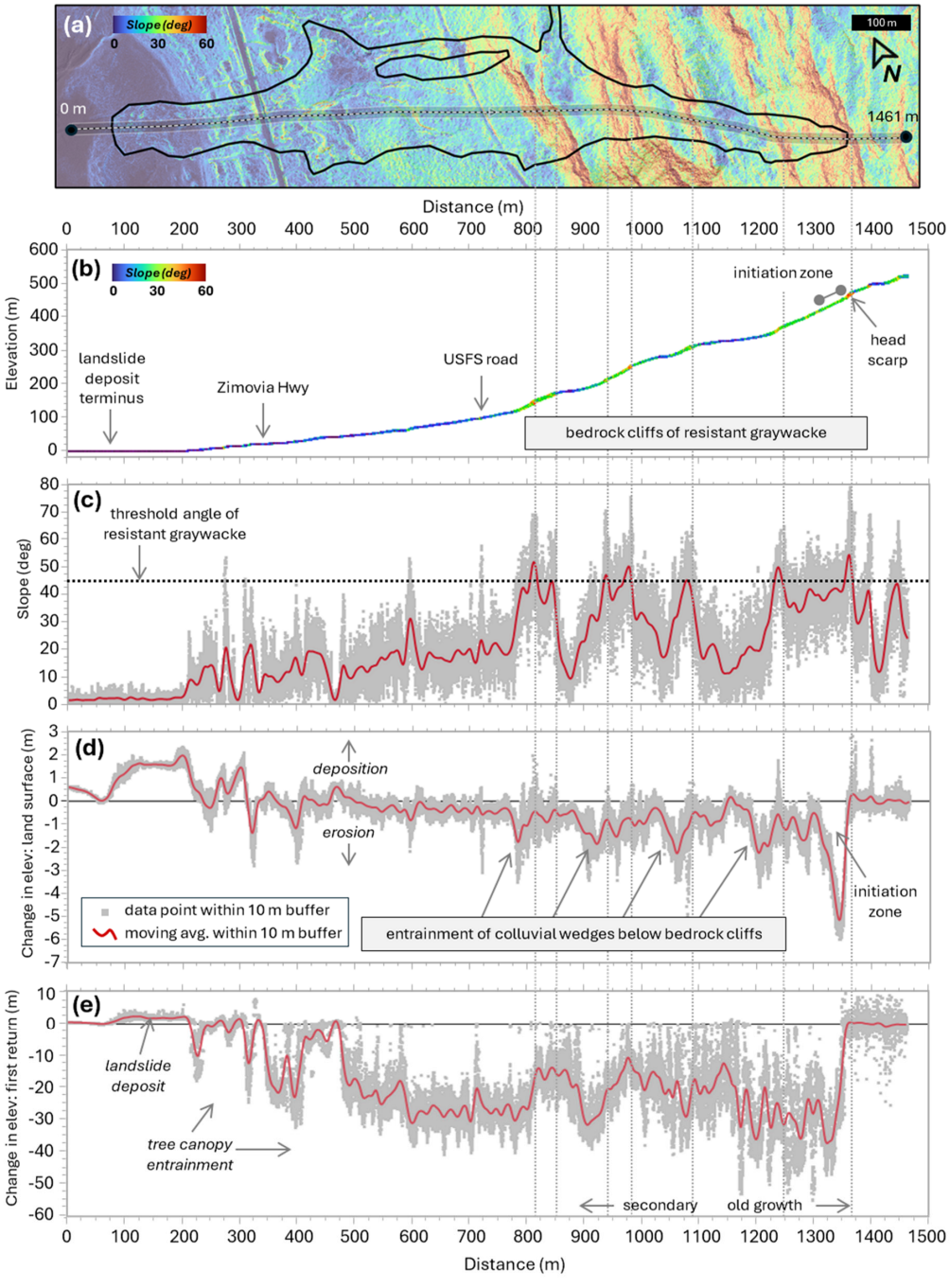

https://doi.org/10.5194/egusphere-2025-4123
Preprint. Discussion started: 9 September 2025

Figure 11. Analysis of landslide properties along a 10-m wide longitudinal transect of the MP11.2 landslide. (**a**) Lidar map of slope angle overlain on shaded relief map with transect location and endpoint distances depicted, (**b**) lidar-derived elevation values from the November 2023 acquisition with points colored by slope angle in degrees, (**c**) lidar-derived slope angle, (**d**) DTM (or land surface) change, and (**e**) DSM (or canopy) change for all points within 10 meters of the transect (gray points) and running average (red line).

Our profile of DTM (or land surface) change shows that net erosion tends to dominate in the upper half of the landslide while negligible net surface change and deposition characterize the lower half (Fig. 11d). The pattern of erosion in the upper half is strongly correlated with the cliff-bench sequences. Specifically, local erosion maxima of 1 to 2 m (denoted by negative values of surface change) span 25 to 50 m horizontally and occur just downslope of the steep bedrock cliffs where they transition to the low-gradient benches (Fig. 11d). These foci of erosion coincide with field observations of colluvial wedges exposed along the lateral margins of the landslide. Our analysis reveals minimal erosion along the low-gradient benches that are situated below these colluvial wedges, and in the field these benches exhibited patchy entrainment as well as minor local deposition. In the field, we also observed a live blueberry patch growing on a subvertical bedrock face at ~1000 m along the transect (Fig. 9c, 11c). This observation implies negligible erosion, and perhaps projectile behaviour of the landslide runout.

The profile of DSM (or canopy) change indicates removal of trees taller than 50 m in the upper 200 m of the initiation and runout zones, whereas trees less than 40 m in height were mobilized from the lower area of the landslide (Fig. 11e). This pattern results from pre-1965 timber harvests along the lower slopes in our study area with the transition to unmanaged forest at 1,100 m along our transect (Fig. 11e). We sampled cookies from four western hemlock trees transported by the landslide and deposited along the slide margins at approximately 900 m along our transect. The violent nature of the landslide snapped the tree trunks, and we estimated that the lower 3 to 5 m of each trunk was missing. To account for the missing record, we added 20 years to the age of each tree. The four trees ranged from 292 ± 10 to 322 ± 10 years old, indicating that they originated from the old growth towards the top of the landslide. We also noted that reaction wood (which can be indicative of slope movement) was present in all tree samples.

We plotted average surface or DTM change against local slope for 10-m intervals along the transect to assess mechanical controls on debris flow entrainment and deposition (Fig. 12). Net erosion dominates when local slope exceeds 15° and the average value of net erosion increases with slope from 15° to 45°. Notably, points defining this trend occur at a wide range of locations along the transect, reflecting the profound influence of local slope on debris entrainment. That said, locations along the middle section of the landslide, which are denoted by filled green circles (Fig. 12), tend to have lower values of net erosion compared to upslope locations, which may result from variations in debris availability or changing inertial forces that control entrainment. For slopes between 41° and 44°, we observed several values of high net erosion (>3 m) that deviate from the local slope-erosion trend. These values (denoted by dark red filled circles and a dashed ellipse in Fig. 12) occur at the uppermost extent of the landslide and are associated with the initiation zone and thus reflect mechanical processes that differ from downslope areas that experienced entrainment. For slope angles less than 15° we observe a trend of increasing deposition with

https://doi.org/10.5194/egusphere-2025-4123
Preprint. Discussion started: 9 September 2025

decreasing slope and a clustering of 0.7 to 1.7 m of deposition at 2° that defines the landslide toe. These trends define the slope-dependent transition between erosion and deposition for runout models, as well as provide constraints on entrainment potential.

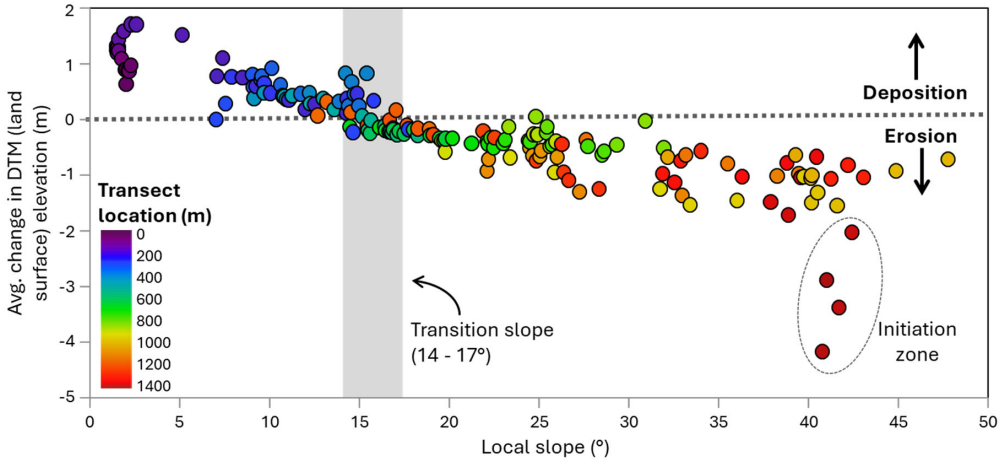

Figure 12. Variation in local net erosion and deposition with slope angle. Values are averaged for 10-m bins along the transect in Fig. 11a. Colours reflect distance along the transect and the vertical grey rectangle denotes the transition slope between erosion and deposition. The dark red points enclosed by a dashed ellipse denote the initiation zone.

We performed a mass balance of erosion and deposition along the MP11.2 landslide to identify the downslope transition of net erosion to deposition and quantify the total volume of erosion and deposition associated with the landslide (Fig. 13). Specifically, we tallied the total thickness of both erosion and deposition for all points within the landslide boundary using 10-m wide swaths oriented perpendicular to the longitudinal transect (Fig. 11a) and then separately summed the values within each swath. The distance between distal points on this transect defines the width of the landslide, which averaged less than 100 m in the upper 500 m of the slide, increased abruptly to greater than 200 m through the middle section, and then decreased to ~100 m in the lower depositional zone (Fig. 13b). Our mass balance analysis indicates high erosion at the initiation zone that decreased downslope before increasing rapidly just above the middle section, which coincides with landslide widening (red line in Fig. 13c). In the lower portions of the wide zone (400 to 500 m along the transect), we observe an abrupt transition from erosion (red line) to deposition (blue line) with a depositional peak that corresponds to the widest section of the landslide. In the field, this zone of localized widening corresponded with extensive accumulation of downed trees on the north flank of the landslide. Substantial deposition is associated with the landslide deposit (located between 75 and 250 m along the transect), just below a zone of local steepness (250 to 350 m along the transect) that experienced efficient transport and minimal deposition or erosion.

https://doi.org/10.5194/egusphere-2025-4123
Preprint. Discussion started: 9 September 2025

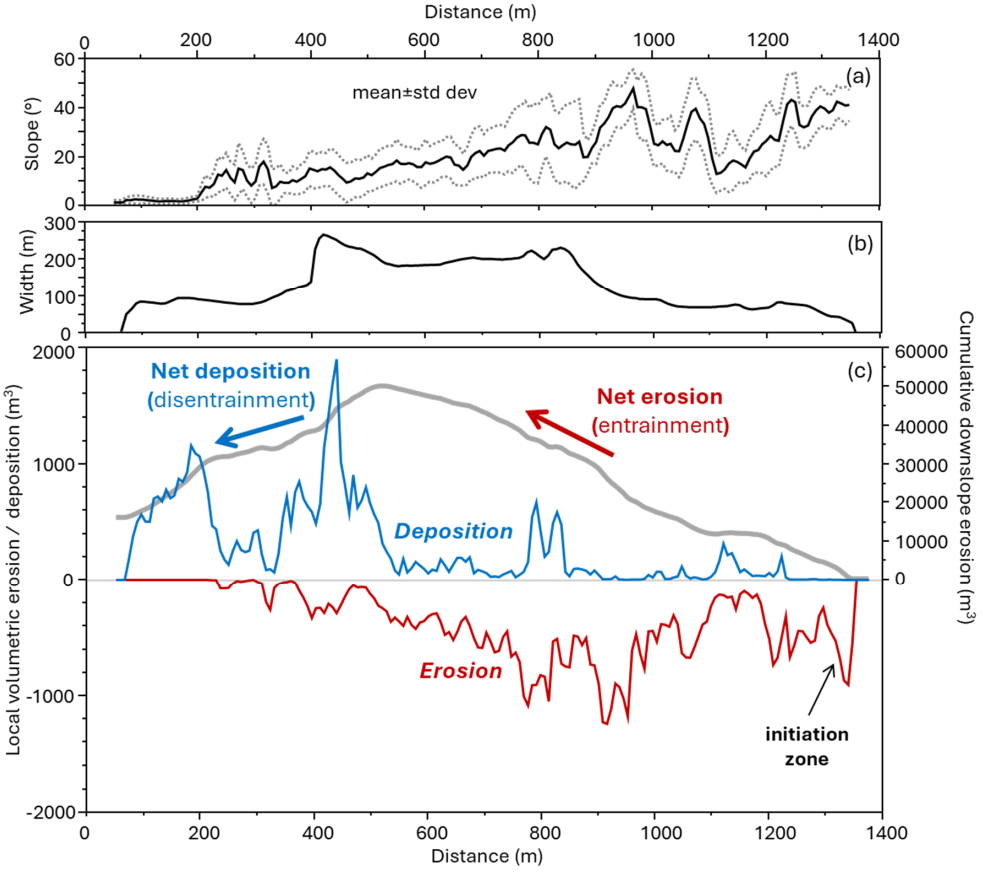

427 **Figure 13.** Downslope mass balance analysis of the MP11.2 landslide. Profiles of (**a**) slope, (**b**) width, and (**c**) local erosion
428 (red), local deposition (blue), and cumulative erosion minus deposition (gray curve) calculated for all points within the
429 landslide boundaries along the transect in Fig. 11a. Note that the northward bifurcation pathway (Fig. 5a) is not included in
430 this analysis.
431
432 Lastly, we integrated total erosion and deposition along the landslide path by starting at the head scarp and summing the
433 imbalance in erosion (positive values of erosion) and deposition (negative values of erosion) in the downslope direction (see
434 grey curve in Fig. 13c), finishing at the slide terminus. Cumulative erosion increases monotonically in the downslope direction
435 before peaking at ~550 m along the transect. This implies an average entrainment rate of 62 $m^3\ m^{-1}$ along the erosional portion
436 of the landslide, although local variations associated with changes in slope occur. Downslope of the net erosion peak, the slide
437 widened substantially, and deposition outpaced erosion downslope. At the slide terminus, the erosion-deposition balance did

https://doi.org/10.5194/egusphere-2025-4123
Preprint. Discussion started: 9 September 2025

not approximate zero, however, indicating that net erosion exceeded deposition. In total, we estimated 65,300 m^3 of erosion and 49,400 m^3 of deposition for the primary landslide, which implies an imbalance of >15,000 m^3 that may reflect debris loss in the coastal deposition zone as well as detection limits in depositional areas and changes in bulk density. For the mass balance of the north-directed bifurcated portion of the landslide (Fig. 5c), we observed 4,000 m^3 of erosion and 3,800 m^3 of deposition.

5 Discussion

5.1 Initiation and triggering factors

Our preliminary investigation indicates that the MP11.2 landslide was an anomalously large and thus long-runout event that initiated in a steep and wide deposit of thick colluvium during a notable but not atypical SE Alaska storm event. A wide range of factors may have affected the initiation of the landslide and the uncertainty ascribed to our interpretations reflects limitations in data availability, chiefly local climate observations, to test landslide initiation hypotheses. By contrast, geomorphic and geologic factors that predisposed the hillslope to landsliding are more straightforward and provide important considerations for the assessment of landslide hazard and risk in other locations.

Initiation of the MP11.2 landslide likely required a high degree of soil saturation to overcome the shear strength of the colluvium and promote the observed highly mobile, fluid-like runout. The rainfall intensity that preceded the landslide was notable but not extraordinary, as quantified by the 1-yr recurrence interval and 3-hr and 6-hr intensities recorded at Wrangell airport. Given the 15-kilometer distance between the airport rain gauge and the landslide, and the greater than 400 m elevation of the initiation zone, the rainfall experienced at MP11.2 is highly uncertain. During our community events, several residents that drove along the Zimovia Highway on November 20 noted that rainfall south of Wrangell and closer to the landslide area was more intense than in the town. In addition, several residents reported the presence of a substantial snowpack at mid- and upper slope locations on the morning of November 20. At the airport weather station at sea level, air temperatures were cold (~2°C) on November 19 and warmed rapidly on the morning of November 20, coincident with the arrival of abundant rainfall. The temporal trend in air temperature at the initiation zone and ridgetop was likely similar although the absolute temperatures were likely lower owing to the higher elevation. As a result, the rapid warming on November 20 combined with hours of moderate-intensity rainfall may have generated substantial runoff via snowmelt. Days after a snow-dominated atmospheric river, an extreme rain-dominated (1 in 500 yr event) atmospheric river generated widespread landslides and the fatal Beach Road landslide in nearby Haines, AK, in December 2020. The scale and impact of these recent events suggest that the sequencing and pacing of snow- and rain-dominated storms may be a critical factor in landslide initiation in SE Alaska. As such, monitoring rain and snow in a wide range of settings is crucial for advancing our understanding of the hydrologic response that contributes to landsliding.

The potential of high wind as a driver of recent landslides across SE Alaska, including the MP11. 2 event, has been surmised by many residents. Tree turnover (or windthrow) can contribute to the initiation of shallow landslides and debris flows based on observations from extreme storms (Guthrie et al., 2010; Lin et al., 2025). Such events tend to trigger widespread windthrow,

https://doi.org/10.5194/egusphere-2025-4123
Preprint. Discussion started: 9 September 2025

however, which was not observed on Wrangell Island during the November 20 storm. In the absence of tree turnover, the potential for trees to transmit dynamic forces into the subsurface due to high winds has not been well-studied. Alternatively, windthrow may impact slope stability through the reduction of root reinforcement (Parra et al., 2021). Pioneering research documenting timber harvest impacts on slope stability was performed in SE Alaska on nearby Prince of Wales Island (Wu et al., 1979) and those studies demonstrated the substantial contribution of soil shear strength through root reinforcement. More recent advances highlight how the progressive tensile loading of root systems in shallow soils undergoing shear can be quantified to assess slope stability in three dimensions, which is critical for capturing how roots reinforce the lateral margins of potentially unstable slopes (Cohen et al., 2009). These studies demonstrate that as soils get thicker, the relative contribution of root reinforcement to the total shear strength decreases substantially given that root density decreases exponentially with depth (Schmidt et al., 2001). The root systems of coniferous forests tend to be concentrated in the upper 1 m (Hales, 2018; Jackson et al., 1996) and as a result, root reinforcement was likely a minor contributor to the cumulative shear resistance of the nearly 5-m thick initiation zone of the MP11.2 landslide. Nonetheless, the contribution may not be negligible, and further analysis of the potential impact of the abating sawfly and budworm infestations on the root systems of western hemlock and Sitka spruce trees in SE Alaska warrants further investigation. The infestation resulted in moderate-to-severe (11-50%) mortality of infested trees on Wrangell Island and impacts are common on west-facing slopes and at elevations that coincide with the initiation zone (U.S. Forest Service, 2025a).

Our field observations of active seepage localized in the SE corner of the MP11.2 head scarp connected to a broad and gentle ridgetop wetland suggests that the extent and character of terrain above steep slopes constitute a key control on landslide susceptibility. Our mapping of hydrologic flowpaths along the ridgeline is consistent with these observations and implies that subtle topographic variability may result in significant changes in the upslope or contributing area of landslide-prone slopes. Similarly, a ponded topographic depression was mapped and monitored upslope of the 2020 Beach Road landslide and narrow channels directly connected that area to the head scarp (Darrow et al., 2022). The abundance of these broad and gentle ridgetops (termed ridgetop water towers) is highly variable across SE Alaska and likely reflects variations in glacial erosion and bedrock properties (Harris et al., 1974). Combining data from the national wetlands inventory with flow routing analyses provides an opportunity to identify these ridgetop drainage systems and characterize those with potential to influence hydrologic response on landslide-prone slopes. Lidar data is a key requirement for characterizing surface hydrology in these environments, and active monitoring of the drainage systems would help determine the magnitude and timescale of hydrologic response and thus the potential contribution to slope instability.

5.2 Geologic and geomorphic factors that condition slopes for failure

An additional factor predisposing the hillslopes above Zimovia Highway to landsliding is the accumulation of thick colluvium that constitutes the initiation zone of the MP11.2 landslide as well as downslope material that enabled entrainment and volumetric growth (or bulking) during runout. The thickness of colluvium varies substantially and systematically across the hillslopes. In the field and from our lidar analyses, we observed extensive colluvial wedges draped below resistant graywacke

https://doi.org/10.5194/egusphere-2025-4123
Preprint. Discussion started: 9 September 2025

layers of the marine sedimentary unit. The punctuated pattern of downslope entrainment highlights how these colluvial wedges contributed to the volumetric growth and broad area of inundation (Fig. 11d). We interpret these deposits to result from progressive post-glacial rockfall locally derived from the resistant and underlying sedimentary layers.

The combination of east-dipping strata and a west-facing hillslope resulted in the observed pattern of bedrock ledges and thick colluvial wedges that characterize much of the area, and we surmise that a non-negligible difference in bedrock strength may be critical for setting up this geomorphic context. Our Schmidt hammer data highlight the high compressive strength of the graywacke and weak strength of the fine-grained inner beds. At a quarry located just north of the landslide, we documented bedrock structure and observed active slaking of the fine-grained inner beds that may destabilize the overlying resistant beds (supplementary materials). Our kinematic analysis showing favourable conditions for flexural toppling is consistent with our interpretation that progressive failure and retreat of the resistant ledges generate a wake of thick colluvium along the hillslopes (Imaizumi et al., 2015). Importantly, these colluvial wedges will continue to form and thicken with on-going rockfall along the resistant cliffs although the pace and frequency of this process is unclear. In nearly all cases, the colluvium is contained within the next downslope bench, which may provide a constraint on the pace of post-glacial bedrock ledge failure and colluvium production. Examination of the TNFLI revealed dozens of other events on Wrangell Island that occurred within a similar geomorphic context. Thus, changes in the bedrock dip and resistance, and slope orientation appear to have a profound effect on the extent and thickness of the colluvial wedges that fueled the MP11.2 landslide, although further investigation is beyond the scope of this contribution.

5.3 Controls on landslide runout and volumetric growth

The large volume and extensive inundation area of the MP11.2 landslide likely originated from a thick and wide initiation zone combined with the entrainment of abundant, saturated colluvium stored on downslope bedrock benches. In this area of SE Alaska, post-glacial isostatic adjustment forms a fringe of uplifted, low-gradient terrain that may provide a key control on landslide runout and deposition. In essence, many landslides on Wrangell and nearby islands appear to terminate upon reaching this low-gradient terrain, when present. Exceptions include particularly large landslides such as MP11.2 and slides that find and follow confined flowpaths, behaving as channelized debris flows. The deposit slope of 2° is substantially lower than values observed on Prince of Wales and Baranof Islands that vary from 4° to 19° and 6° to 26°, respectively (Booth et al., 2020; Johnson et al., 2000). Given that the mobility value (H/L~0.45) for the MP11.2 slide is not anomalous (Fig. 7a), we interpret its low deposit angle, and thus outsized and tragic impact, to result from highly efficient entrainment and volumetric growth, which resulted in a large area and volume. Experimental and theoretical investigations of debris flow runout emphasize that pore pressures generated as wet bed sediment is overridden and progressively entrained, can reduce friction and facilitate increases in flow momentum (Iverson et al., 2011; Reid, 2011). Furthermore, because the colluvial stores on the slope were emplaced by rockfall activity and soil transport, they may exist in a contractive state such that deformation and shearing facilitate pore pressure development and volumetric growth.

https://doi.org/10.5194/egusphere-2025-4123
Preprint. Discussion started: 9 September 2025

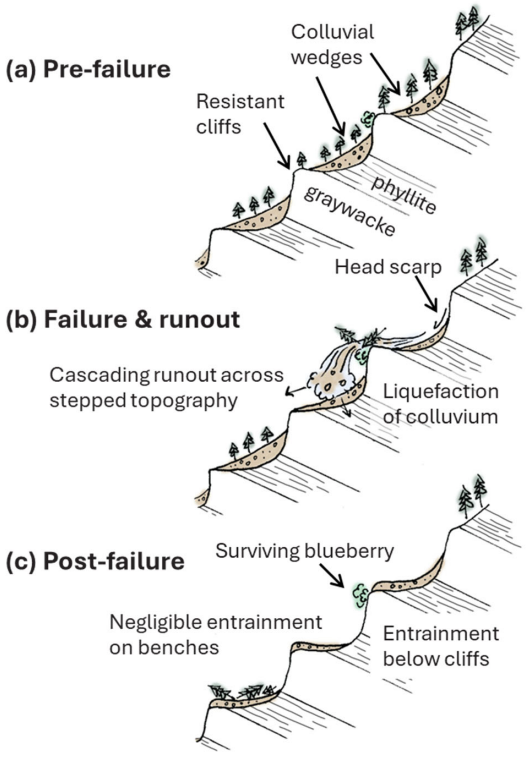

Figure 14. Schematic of (**a**) pre-, (**b**) syn-, and (**c**) post-slide hillslope geometry, highlighting the influence of resistant bedrock and the downslope accumulation of colluvium that becomes mobilized during the landslide event. The live blueberry bush below a resistant bed reveals cascading, projectile-like behaviour of the slide material.

The linear entrainment rate of 62 m^3 m^{-1} is nearly 10x higher than typical values in unglaciated terrain (Reid et al., 2016), highlighting the importance of unconsolidated sediment thickness on steep slopes for determining landslide volume. From a mechanistic standpoint, the sequence of subvertical bedrock cliffs along the slide path also suggests that dynamic loading of stored colluvium from falling debris may have led to undrained loading and liquefaction (Collins and Reid, 2020). Thus, the sequence of steps may have facilitated momentum growth through a series of loading-induced liquefaction events (Fig. 14). This behaviour has been noted in other highly-mobile landslides with extensive inundation zones (Iverson et al., 2015). Lastly, the 15° slope angle that governs the transition between erosion and deposition along the MP11.2 landslide is steeper than values observed in unglaciated terrain that features valley confinement and thus enables long runout debris flows. Acquiring

https://doi.org/10.5194/egusphere-2025-4123
Preprint. Discussion started: 9 September 2025

estimates of this transition slope is necessary for implementing landslide runout models, such as Laharz and GrfinTools (Brien et al., 2025) and will advance our ability to predict landslide impacts in the region.

6 Conceptual framework and research needs for shallow landslide assessment in SE Alaska

Our analysis highlights key factors that govern the behaviour and hazard potential of shallow landslides in post-glacial landscapes, such as SE Alaska.

- First, the accumulation of colluvium (or soil) on steep hillslopes serves as a key conditioning process for slope instability. Previous studies in SE Alaska indicate typical landslide depths of 0.5 to 2.0 m and invoke in-situ weathering of glacial till, soil creep, and tephra deposition as processes that generate material of sufficient thickness to initiate shallow landslides. Here, we identify deposition of thick colluvial wedges below resistant bedrock cliffs as an additional contributor, although the relative importance of these processes remains unclear. More generally, the timescale of processes that generate colluvium dictates the frequency, magnitude, and spatial pattern of landsliding in post-glacial landscapes although relevant data are limited.
- Second, characterizing water sources and flow accumulation above landslide-prone hillslopes will facilitate the identification of terrain with high hazard potential. Many glaciated mountains feature broad, gentle ridgetops that can store and convey large quantities of surface and near-surface water, particularly during snowmelt and rain-on-snow events. In British Columbia, this terrain is termed “gentle-over-steep” (Jordan, 2016) and efforts to characterize and map these particular landforms and quantify drainage patterns using airborne lidar data should be a research priority in SE Alaska.
- Third, the runout of debris flows and debris avalanches in SE Alaska is seldom facilitated by channels or topographic confinement. Rather, most landslides navigate poorly-dissected, post-glacial terrain, and the prediction of debris flow runout in these settings is challenging owing to highly-variable resistance in the form of vegetation and flow materials. In these post-glacial settings, the parameters for empirical models (such as the erosion-deposition transition angle) have not been constrained and the ability of these models to account for controls on runout is untested. Physically-based models that account for how large wood and variable grain size dictate flow behaviour also merit further investigation in conjunction with landslide inventory data and field observations.
- Fourth, because debris flow volume is the primary control on inundation area, quantification of entrainment along slide paths is essential for runout modelling. The availability of colluvium and its relative saturation can promote entrainment. Spatial and temporal variations in these two factors likely depend on the pace and pattern of post-glacial landscape evolution that determines where colluvium accumulates and how hillslope drainage paths are organized. Thus, landscape evolution models that are developed and tested in postglacial settings should be a research priority.
- Lastly, although atmospheric rivers have been responsible for all the recent fatal landslide events in SE Alaska, the character and relative magnitude of these ARs have been highly variable. Some have been notable for producing a

https://doi.org/10.5194/egusphere-2025-4123
Preprint. Discussion started: 9 September 2025

few hours of intense rainfall while others have been characterized by protracted rain-on-snow. Thus, quantifying how the sequencing and character of ARs affects landslide susceptibility will be a key component of efforts to build a landslide warning system (Nash et al., 2024). Currently, the region lacks sufficient weather station observations and climate reanalysis productions (Lader et al., 2020) are limited in scope and resolution.

Most generally, advancing our understanding of how these geomorphic and atmospheric processes contribute to slope instability across SE Alaska will inform how we assess, plan, mitigate, and manage landslide hazards and minimize impacts on public safety and infrastructure.

7 Conclusions

The 2023 Wrangell Island landslide was among the most impactful and deadly in Southeast Alaska's recent history and reveals critical insights into shallow landslide processes in post-glacial terrain. Our investigation demonstrates how geological structure, post-glacial landscape evolution, hydrologic connectivity, and atmospheric forcing combined to produce a high-impact event with devastating consequences. Although rainfall intensity during the triggering storm was relatively modest, the landslide magnitude and impact were amplified by several preconditioning factors that are poorly represented with existing conceptual models and hazard frameworks.

Our key findings include the following:

- Evidence of extensive windthrow contributing to the slope failure is lacking, but rain-on-snow dynamics may have delivered critical runoff not captured by typical rainfall intensity metrics.
- Ridgetop wetlands with subtle drainage divides control hydrologic routing to many landslide-prone slopes, concentrating surface flowpaths and downslope slope saturation.
- Thick colluvial wedges, perched below resistant bedrock ledges, provided an abundant source zone of readily mobilized material that fuelled entrainment and long runout.
- Stepped topography acted to maintain flow momentum, enabling progressive entrainment and promoting mobility.
- Sequential lidar and flow modelling are essential tools for identifying landslide initiation susceptibility, erosion/deposition patterns, and geomorphic preconditioning.
- Large, high mobility shallow landslides can occur on anti-dip hillslopes and risk may be greater than previously recognized.

These findings highlight high key knowledge gaps and can guide future risk mitigation and early warning strategies in steep, post-glacial landscapes. Specifically, advancing landslide prediction in SE Alaska requires expanded lidar coverage, integrated snow and rainfall monitoring, climate modelling, and advances in the modelling of post-glacial landscape evolution, weathering, and colluvium thickness that provide the means for landslide initiation and entrainment.

https://doi.org/10.5194/egusphere-2025-4123
Preprint. Discussion started: 9 September 2025

8 Acknowledgments

The authors thank the National Science Foundation (RAPID EAR Award 2421234) for supporting this work, Wrangell Cooperative Association for partnership and knowledge sharing, City of Wrangell staff for resources, discussions, and maps, S. and G. Helgesen for access, A. Park and A. Edwards for fieldwork contributions, A. O'Brien and T. Belback for their excellent sawyer services, and Nolan Center staff for hosting multiple community events.

References

Alaska Department of Transportation and Public Facilities: Alaska Test Methods Manual: ADOT&PF, 2023.

American Society for Testing Materials: Standard Test Method for Determination of Rock Hardness by Rebound Hammer Method, 2014a.

American Society for Testing Materials: Standard Test Methods for Specific Gravity of Soil Solids by Water Pycnometer, 2014b.

American Society for Testing Materials: Standard Practice for Classification of Soils for Engineering Purposes (Unified Soil Classification System), 2017a.

American Society for Testing Materials: Standard Test Methods for Particle-Size Distribution (Gradation) of Soils Using Sieve Analysis, 2017b.

American Society for Testing Materials: Standard Test Method for Particle-Size Distribution (Gradation) of Fine-Grained Soils Using the Sedimentation (Hydrometer) Analysis, 2021.

Aydin, A. and Basu, A.: The Schmidt hammer in rock material characterization, Engineering Geology, 81, 1–14, https://doi.org/10.1016/j.enggeo.2005.06.006, 2005.

Baichtal, J. F., Lesnek, A. J., Carlson, R. J., Schmuck, N. S., Smith, J. L., Landwehr, D. J., and Briner, J. P.: Late Pleistocene and early Holocene sea-level history and glacial retreat interpreted from shell-bearing marine deposits of southeastern Alaska, USA, Geosphere, 17, 1590–1615, https://doi.org/10.1130/GES02359.1, 2021.

Benda, L. and Dunne, T.: Stochastic forcing of sediment supply to channel networks from landsliding and debris flow, Water Resources Research, 33, 2849–2863, https://doi.org/10.1029/97WR02388, 1997.

Booth, A. M., Sifford, C., Vascik, B., Siebert, C., and Buma, B.: Large wood inhibits debris flow runout in forested southeast Alaska, Earth Surface Processes and Landforms, n/a, https://doi.org/10.1002/esp.4830, 2020.

Booth, A. M., Buma, B., and Nagorski, S.: Effects of Landslides on Terrestrial Carbon Stocks With a Coupled Geomorphic-Biologic Model: Southeast Alaska, United States, Journal of Geophysical Research: Biogeosciences, 128, e2022JG007297, https://doi.org/10.1029/2022JG007297, 2023.

Bovy, B., Braun, J., and Demoulin, A.: A new numerical framework for simulating the control of weather and climate on the evolution of soil-mantled hillslopes, Geomorphology, 263, 99–112, https://doi.org/10.1016/j.geomorph.2016.03.016, 2016.

https://doi.org/10.5194/egusphere-2025-4123
Preprint. Discussion started: 9 September 2025

642 Brardinoni, F. and Hassan, M. A.: Glacial erosion, evolution of river long profiles, and the organization of process domains in
643 mountain drainage basins of coastal British Columbia, Journal of Geophysical Research, 111,
644 https://doi.org/10.1029/2005JF000358, 2006.

645 Brardinoni, F., Hassan, M. A., Rollerson, T., and Maynard, D.: Colluvial sediment dynamics in mountain drainage basins,
646 Earth and Planetary Science Letters, 284, 310–319, https://doi.org/10.1016/j.epsl.2009.05.002, 2009.

647 Brardinoni, F., Picotti, V., Maraio, S., Bruno, P. P., Cucato, M., Morelli, C., and Mair, V.: Postglacial evolution of a formerly
648 glaciated valley: Reconstructing sediment supply, fan building, and confluence effects at the millennial time scale, GSA
649 Bulletin, 130, 1457–1473, https://doi.org/10.1130/B31924.1, 2018.

650 Brien, D. L., Reid, M. E., Cronkite-Ratcliff, C., and Perkins, J. P.: Topographic controls on landslide mobility: modeling
651 hurricane-induced landslide runout and debris-flow inundation in Puerto Rico, Natural Hazards and Earth System Sciences,
652 25, 1229–1253, https://doi.org/10.5194/nhess-25-1229-2025, 2025.

653 Buma, B. and Johnson, A. C.: The role of windstorm exposure and yellow cedar decline on landslide susceptibility in southeast
654 Alaskan temperate rainforests, Geomorphology, 228, 504–511, https://doi.org/10.1016/j.geomorph.2014.10.014, 2015.

655 Buma, B. and Pawlik, Ł.: Post-landslide soil and vegetation recovery in a dry, montane system is slow and patchy, Ecosphere,
656 12, https://doi.org/10.1002/ecs2.3346, 2021.

657 Carrara, P. E., Ager, T. A., Baichtal, J. F., and VanSistine, D. P.: Map of glacial limits and possible refugia in the southern
658 Alexander Archipelago, Alaska, during the late Wisconsin glaciation, Miscellaneous Field Studies Map,
659 https://doi.org/10.3133/mf2424, 2003.

660 Cohen, D., Lehmann, P., and Or, D.: Fiber bundle model for multiscale modeling of hydromechanical triggering of shallow
661 landslides, Water Resources Research, 45, https://doi.org/10.1029/2009WR007889, 2009.

662 Collins, B. D. and Reid, M. E.: Enhanced landslide mobility by basal liquefaction: The 2014 State Route 530 (Oso),
663 Washington, landslide, GSA Bulletin, 132, 451–476, https://doi.org/10.1130/B35146.1, 2020.

664 Cordeira, J. M., Stock, J., Dettinger, M. D., Young, A. M., Kalansky, J. F., and Ralph, F. M.: A 142-year Climatology of
665 Northern California Landslides and Atmospheric Rivers, Bulletin of the American Meteorological Society, BAMS-D-18-
666 0158.1, https://doi.org/10.1175/BAMS-D-18-0158.1, 2019.

667 Darrow, M. M., Nelson, V. A., Grilliot, M., Wartman, J., Jacobs, A., Baichtal, J. F., and Buxton, C.: Geomorphology and
668 initiation mechanisms of the 2020 Haines, Alaska landslide, Landslides, https://doi.org/10.1007/s10346-022-01899-3, 2022.

669 DiBiase, R. A., Lamb, M. P., Ganti, V., and Booth, A. M.: Slope, grain size, and roughness controls on dry sediment transport
670 and storage on steep hillslopes: PARTICLE TRANSPORT ON STEEP HILLSLOPES, Journal of Geophysical Research:
671 Earth Surface, 122, 941–960, https://doi.org/10.1002/2016JF003970, 2017.

672 Dietrich, W. E., Wilson, C. J., and Reneau, S. L.: Hollows, colluvium, and landslides in soil-mantled landscapes, in: Hillslope
673 Processes, edited by: Abrahams, A. D., Routledge, 362–388, https://doi.org/10.4324/9781003028840-17, 1986.

674 Dietrich, W. E., Reiss, R., Hsu, M., and Montgomery, D. R.: A process-based model for colluvial soil depth and shallow
675 landsliding using digital elevation data, Hydrological Processes, 9, 383–400, https://doi.org/10.1002/hyp.3360090311, 1995.

676 D'Odorico, P. and Fagherazzi, S.: A probabilistic model of rainfall-triggered shallow landslides in hollows: A long-term
677 analysis, Water Resources Research, 39, https://doi.org/10.1029/2002WR001595, 2003.

https://doi.org/10.5194/egusphere-2025-4123
Preprint. Discussion started: 9 September 2025

678 Fan, L., Lehmann, P., Zheng, C., and Or, D.: Rainfall Intensity Temporal Patterns Affect Shallow Landslide Triggering and
679 Hazard Evolution, Geophysical Research Letters, 47, e2019GL085994, https://doi.org/10.1029/2019GL085994, 2020.

680 Flagstad, L., Steer, A., Boucher, T., Aisu, M., and Lema, P.: Wetlands across Alaska: Statewide wetland map and Assessment
681 of rare wetland ecosystems, 2018.

682 Gabet, E. J. and Mudd, S. M.: The mobilization of debris flows from shallow landslides, Geomorphology, 74, 207–218,
683 https://doi.org/10.1016/j.geomorph.2005.08.013, 2006.

684 Godt, J. W., Wood, N. J., Pennaz, A. B., Dacey, C. M., Mirus, B. B., Schaefer, L. N., and Slaughter, S. L.: National strategy
685 for landslide loss reduction, Open-File Report, U.S. Geological Survey, https://doi.org/10.3133/ofr20221075, 2022.

686 Goetz, J. N., Guthrie, R. H., and Brenning, A.: Forest harvesting is associated with increased landslide activity during an
687 extreme rainstorm on Vancouver Island, Canada, Natural Hazards and Earth System Sciences, 15, 1311–1330,
688 https://doi.org/10.5194/nhess-15-1311-2015, 2015.

689 Gonzalez de Vallejo, L. and Ferrer, M.: Geological Engineering, CRC Press, London, 700 pp., https://doi.org/10.1201/b11745,
690 2011.

691 Gorr, A. N., McGuire, L. A., Youberg, A. M., and Rengers, F. K.: A progressive flow-routing model for rapid assessment of
692 debris-flow inundation, Landslides, 19, 2055–2073, https://doi.org/10.1007/s10346-022-01890-y, 2022.

693 Guilinger, J. J., Foufoula-Georgiou, E., Gray, A. B., Randerson, J. T., Smyth, P., Barth, N. C., and Goulden, M. L.: Predicting
694 Postfire Sediment Yields of Small Steep Catchments Using Airborne Lidar Differencing, Geophysical Research Letters, 50,
695 e2023GL104626, https://doi.org/10.1029/2023GL104626, 2023.

696 Guthrie, R. H.: The effects of logging on frequency and distribution of landslides in three watersheds on Vancouver Island,
697 British Columbia, Geomorphology, 43, 273–292, https://doi.org/10.1016/S0169-555X(01)00138-6, 2002.

698 Guthrie, R. H., Mitchell, S. J., Lanquaye-Opoku, N., and Evans, S. G.: Extreme weather and landslide initiation in coastal
699 British Columbia, Quarterly Journal of Engineering Geology and Hydrogeology, 43, 417–428, https://doi.org/10.1144/1470-
700 9236/08-119, 2010.

701 Haeussler, P. J.: Structural evolution of an arc-basin: The Gravina Belt in central southeastern Alaska, Tectonics, 11, 1245–
702 1265, https://doi.org/10.1029/92TC01107, 1992.

703 Hales, T. C.: Modelling biome-scale root reinforcement and slope stability, Earth Surface Processes and Landforms, 43, 2157–
704 2166, https://doi.org/10.1002/esp.4381, 2018.

705 Hamilton, T. D.: Late Cenozoic glaciation of Alaska, in: The Geology of Alaska, vol. G-1, edited by: Plafker, G. and Berg, H.
706 C., Geological Society of America, 0, https://doi.org/10.1130/DNAG-GNA-G1.813, 1994.

707 Harris, A. S. and Farr, W. A.: The forest ecosystem of southeast Alaska: 7. Forest ecology and timber management., Gen.
708 Tech. Rep. PNW-GTR-025. Portland, OR: U.S. Department of Agriculture, Forest Service, Pacific Northwest Research
709 Station. 116 p, 025, 1974.

710 Harris, A. S., Hutchison, K., Meehan, W. R., Swanston, D. N., Helmers, A. E., Hendee, J. C., and Collins, T. M.: THE FOREST
711 ECOSYSTEM OF SOUTHEAST ALASKA l.The Setting, USDA, Portland, OR, 1974.

https://doi.org/10.5194/egusphere-2025-4123
Preprint. Discussion started: 9 September 2025

712 Hees, W. W. S. van and Mead, B. R.: Extensive, strategic assessment of southeast Alaska's vegetative resources., Landscape
713 and Urban Planning. 72: 25-48, https://doi.org/10.1016/j.landurbplan.2004.09.027, 2005.

714 Hovius, N., Stark, C. P., and Allen, P. A.: Sediment flux from a mountain belt derived by landslide mapping, Geology, 25,
715 231, https://doi.org/10.1130/0091-7613(1997)025%253C0231:SFFAMB%253E2.3.CO;2, 1997.

716 Howe, M., Graham, E. E., and Nelson, K. N.: Defoliator outbreaks track with warming across the Pacific coastal temperate
717 rainforest of North America, Ecography, 2024, e07370, https://doi.org/10.1111/ecog.07370, 2024.

718 Imaizumi, F., Nishii, R., Murakami, W., and Daimaru, H.: Parallel retreat of rock slopes underlain by alternation of strata,
719 Geomorphology, 238, 27–36, https://doi.org/10.1016/j.geomorph.2015.02.030, 2015.

720 Iverson, R. M.: Landslide triggering by rain infiltration, Water Resour. Res., 36, 1897–1910,
721 https://doi.org/10.1029/2000WR900090, 2000.

722 Iverson, R. M. and Ouyang, C.: Entrainment of bed material by Earth-surface mass flows: Review and reformulation of depth-
723 integrated theory: Entrainment of bed material, Reviews of Geophysics, 53, 27–58, https://doi.org/10.1002/2013RG000447,
724 2015.

725 Iverson, R. M., Reid, M. E., Logan, M., LaHusen, R. G., Godt, J. W., and Griswold, J. P.: Positive feedback and momentum
726 growth during debris-flow entrainment of wet bed sediment, Nature Geosci, 4, 116–121, https://doi.org/10.1038/ngeo1040,
727 2011.

728 Iverson, R. M., George, D. L., Allstadt, K., Reid, M. E., Collins, B. D., Vallance, J. W., Schilling, S. P., Godt, J. W., Cannon,
729 C. M., Magirl, C. S., Baum, R. L., Coe, J. A., Schulz, W. H., and Bower, J. B.: Landslide mobility and hazards: implications
730 of the 2014 Oso disaster, Earth and Planetary Science Letters, 412, 197–208, https://doi.org/10.1016/j.epsl.2014.12.020, 2015.

731 Jackson, R. B., Canadell, J., Ehleringer, J. R., Mooney, H. A., Sala, O. E., and Schulze, E. D.: A global analysis of root
732 distributions for terrestrial biomes, Oecologia, 108, 389–411, https://doi.org/10.1007/BF00333714, 1996.

733 Johnson, A. C., Swanston, D. N., and McGee, K. E.: LANDSLIDE INITIATION, RUNOUT, AND DEPOSITION WITHIN
734 CLEARCUTS AND OLD-GROWTH FORESTS OF ALASKA [1], J American Water Resour Assoc, 36, 17–30,
735 https://doi.org/10.1111/j.1752-1688.2000.tb04245.x, 2000.

736 Jordan, P.: Post-wildfire debris flows in southern British Columbia, Canada, Int. J. Wildland Fire, 25, 322,
737 https://doi.org/10.1071/WF14070, 2016.

738 Karl, S. M., Haeussler, P. J., and Mccafferty, A. E.: Reconnaissance Geologic Map of the Duncan Canal/Zarembo Island Area,
739 Southeastern Alaska, Reston, VA, 1999.

740 Korup, O., Densmore, A. L., and Schlunegger, F.: The role of landslides in mountain range evolution, Geomorphology, 120,
741 77–90, https://doi.org/10.1016/j.geomorph.2009.09.017, 2010.

742 Lader, R., Bidlack, A., Walsh, J. E., Bhatt, U. S., and Bieniek, P. A.: Dynamical Downscaling for Southeast Alaska: Historical
743 Climate and Future Projections, https://doi.org/10.1175/JAMC-D-20-0076.1, 2020.

744 Lamb, M. P., Scheingross, J. S., Amidon, W. H., Swanson, E., and Limaye, A.: A model for fire-induced sediment yield by
745 dry ravel in steep landscapes, Journal of Geophysical Research, 116, https://doi.org/10.1029/2010JF001878, 2011.

https://doi.org/10.5194/egusphere-2025-4123
Preprint. Discussion started: 9 September 2025

Lancaster, S. T., Hayes, S. K., and Grant, G. E.: Effects of wood on debris flow runout in small mountain watersheds: EFFECTS OF WOOD ON DEBRIS FLOW RUNOUT, Water Resources Research, 39, https://doi.org/10.1029/2001WR001227, 2003.

Larsen, I. J., Montgomery, D. R., and Korup, O.: Landslide erosion controlled by hillslope material, Nature Geoscience, 3, 247–251, https://doi.org/10.1038/ngeo776, 2010.

Lempert, R. J., Busch, L., Brown, R., Patton, A., Turner, S., Schmidt, J., and Young, T.: Community-Level, Participatory Co-Design for Landslide Warning with Implications for Climate Services, Sustainability, 15, 4294, https://doi.org/10.3390/su15054294, 2023.

Lin, Y.-C., Hsieh, J.-Y., Shih, H.-S., and Wang, W.-H.: Strong wind is one of the important factors that trigger landslides, npj Nat. Hazards, 2, 12, https://doi.org/10.1038/s44304-025-00062-x, 2025.

Mann, D. H. and Hamilton, T. D.: Late Pleistocene and Holocene paleoenvironments of the North Pacific coast, Quaternary Science Reviews, 14, 449–471, https://doi.org/10.1016/0277-3791(95)00016-I, 1995.

Marra, F., Armon, M., and Morin, E.: Coastal and orographic effects on extreme precipitation revealed by weather radar observations, Hydrology and Earth System Sciences, 26, 1439–1458, https://doi.org/10.5194/hess-26-1439-2022, 2022.

Menounos, B., Goehring, B. M., Osborn, G., Margold, M., Ward, B., Bond, J., Clarke, G. K. C., Clague, J. J., Lakeman, T., Koch, J., Caffee, M. W., Gosse, J., Stroeven, A. P., Seguinot, J., and Heyman, J.: Cordilleran Ice Sheet mass loss preceded climate reversals near the Pleistocene Termination, Science, 358, 781–784, https://doi.org/10.1126/science.aan3001, 2017.

Montgomery, D. R., Dietrich, W. E., Torres, R., Anderson, S. P., Heffner, J. T., and Loague, K.: Hydrologic response of a steep, unchanneled valley to natural and applied rainfall, Water Resour. Res., 33, 91–109, https://doi.org/10.1029/96WR02985, 1997.

Nash, D., Rutz, J. J., and Jacobs, A.: Atmospheric Rivers in Southeast Alaska: Meteorological Conditions Associated With Extreme Precipitation, Journal of Geophysical Research: Atmospheres, 129, e2023JD039294, https://doi.org/10.1029/2023JD039294, 2024.

National Oceanographic and Atmospheric Administration (NOAA): NOWData – NOAA Online Weather Data, 2024.

Neiman, P. J., Ralph, F. M., Wick, G. A., Lundquist, J. D., and Dettinger, M. D.: Meteorological Characteristics and Overland Precipitation Impacts of Atmospheric Rivers Affecting the West Coast of North America Based on Eight Years of SSM/I Satellite Observations, Journal of Hydrometeorology, 9, 22–47, https://doi.org/10.1175/2007JHM855.1, 2008.

Nicolazzo, J. A., Wikstrom Jones, K. M., Salisbury, J. B., and Horen, K. C.: Post-landslide elevation changes detected from multi-temporal lidar surveys of the November 2023 Wrangell, Alaska, landslides, Alaska Division of Geological & Geophysical Surveys, https://doi.org/10.14509/31124, 2024.

Oakley, N. S., Lancaster, J. T., Hatchett, B. J., Stock, J., Ralph, F. M., Roj, S., and Lukashov, S.: A 22-Year Climatology of Cool Season Hourly Precipitation Thresholds Conducive to Shallow Landslides in California, Earth Interact., 22, 1–35, https://doi.org/10.1175/EI-D-17-0029.1, 2018.

Parra, E., Mohr, C. H., and Korup, O.: Predicting Patagonian Landslides: Roles of Forest Cover and Wind Speed, Geophysical Research Letters, 48, e2021GL095224, https://doi.org/10.1029/2021GL095224, 2021.

https://doi.org/10.5194/egusphere-2025-4123
Preprint. Discussion started: 9 September 2025

781 Patton, A. I., Roering, J. J., and Orland, E.: Debris flow initiation in postglacial terrain: Insights from shallow landslide
782 initiation models and geomorphic mapping in Southeast Alaska, Earth Surface Processes and Landforms, n/a,
783 https://doi.org/10.1002/esp.5336, 2022.

784 Patton, A. I., Luna, L. V., Roering, J. J., Jacobs, A., Korup, O., and Mirus, B. B.: Landslide initiation thresholds in data-sparse
785 regions: application to landslide early warning criteria in Sitka, Alaska, USA, Natural Hazards and Earth System Sciences, 23,
786 3261–3284, https://doi.org/10.5194/nhess-23-3261-2023, 2023.

787 Ralph, F. M., Neiman, P. J., and Wick, G. A.: Satellite and CALJET Aircraft Observations of Atmospheric Rivers over the
788 Eastern North Pacific Ocean during the Winter of 1997/98, 2004.

789 Reid, M. E.: Entrainment of bed sediment by debris flows : results from large-scale experiments, Italian Journal of Engineering
790 Geology and Environment, 367–374, https://doi.org/10.4408/IJEGE.2011-03.B-042, 2011.

791 Reid, M. E., Coe, J. A., and Brien, D. L.: Forecasting inundation from debris flows that grow volumetrically during travel,
792 with application to the Oregon Coast Range, USA, Geomorphology, 273, 396–411,
793 https://doi.org/10.1016/j.geomorph.2016.07.039, 2016.

794 Rengers, F. K., Kean, J. W., Reitman, N. G., Smith, J. B., Coe, J. A., and McGuire, L. A.: The Influence of Frost Weathering
795 on Debris Flow Sediment Supply in an Alpine Basin, Journal of Geophysical Research: Earth Surface, 125, e2019JF005369,
796 https://doi.org/10.1029/2019JF005369, 2020.

797 Rickenmann, D.: Empirical Relationships for Debris Flows, Natural Hazards, 19, 47–77,
798 https://doi.org/10.1023/A:1008064220727, 1999.

799 Rulli, M. C., Meneguzzo, F., and Rosso, R.: Wind control of storm-triggered shallow landslides, Geophysical Research Letters,
800 34, https://doi.org/10.1029/2006GL028613, 2007.

801 Schmidt, K. M., Roering, J. J., Stock, J. D., Dietrich, W. E., Montgomery, D. R., and Schaub, T.: The variability of root
802 cohesion as an influence on shallow landslide susceptibility in the Oregon Coast Range, Canadian Geotechnical Journal, 38,
803 995–1024, https://doi.org/10.1139/cgj-38-5-995, 2001.

804 Schuster, R. L. and Highland, L. M.: Socioeconomic and environmental impacts of landslides in the Western Hemisphere,
805 https://doi.org/10.3133/ofr01276, 2001.

806 Schwanghart, W. and Scherler, D.: Short Communication: TopoToolbox 2 – MATLAB-based software for topographic
807 analysis and modeling in Earth surface sciences, Earth Surface Dynamics, 2, 1–7, https://doi.org/10.5194/esurf-2-1-2014,
808 2014.

809 Sharma, A. R. and Déry, S. J.: Contribution of Atmospheric Rivers to Annual, Seasonal, and Extreme Precipitation Across
810 British Columbia and Southeastern Alaska, J. Geophys. Res. Atmos., 125, https://doi.org/10.1029/2019JD031823, 2020.

811 Spinola, D., Margerum, A., Zhang, Y., Hesser, R., D'Amore, D., and Portes, R.: Rapid soil formation and carbon accumulation
812 along a Little Ice Age soil chronosequence in southeast Alaska, CATENA, 246, 108460,
813 https://doi.org/10.1016/j.catena.2024.108460, 2024.

814 Stock, J. and Dietrich, W. E.: Valley incision by debris flows: Evidence of a topographic signature: VALLEY INCISION BY
815 DEBRIS FLOWS, Water Resources Research, 39, https://doi.org/10.1029/2001WR001057, 2003.

https://doi.org/10.5194/egusphere-2025-4123
Preprint. Discussion started: 9 September 2025

816 Swanson, F. J., Benda, L. E., Duncan, S. H., Grant, G. E., Megahan, W. F., Reid, L. M., and Ziemer, R. R.: Mass failures and
817 other processes of sediment production in Pacific northwest forest landscapes, Pages 9-38, in: Ernest O. Salo and Terrance W.
818 Cundy (eds.), Streamside Management: Forestry and Fishery Interactions, Proceedings of a Symposium held at University of
819 Washington, 12-14 February 1986. Contribution no. 57, Institute of Forest Resources, Seattle, Washington., 1987.

820 Swanston, D. N.: Mass Wasting in Coastal Alaska, USFS Technical Report, 1969.

821 Swanston, D. N.: Mechanics of Avalanching in Shallow till soils of SE Alaska, Juneau, AK, 1970.

822 Swanston, D. N.: Judging Landslide Potential in Glaciated Valleys of Southeastern Alaska, Explorers, 4, 1973.

823 U.S. Forest Service: Satellite-based Change Detection Southeast Alaska, 2025a.

824 U.S. Forest Service: Tongass Landslide Areas: Data.gov, 2025b.

825 Vascik, B. A., Booth, A. M., Buma, B., and Berti, M.: Estimated Amounts and Rates of Carbon Mobilized by Landsliding in
826 Old-Growth Temperate Forests of SE Alaska, JGR Biogeosciences, 126, https://doi.org/10.1029/2021JG006321, 2021.

827 Wendler, G., Galloway, K., and Stuefer, M.: On the climate and climate change of Sitka, Southeast Alaska, Theor Appl
828 Climatol, 126, 27–34, https://doi.org/10.1007/s00704-015-1542-7, 2016.

829 Wheeler, J. O. and McFeely, P.: Tectonic assemblage map of the Canadian Cordillera and adjacent parts of the United States
830 of America, 1991.

831 Wu, T. H., McKinnell III, W. P., and Swanston, D. N.: Strength of tree roots and landslides on Prince of Wales Island, Alaska,
832 Can. Geotech. J., 16, 19–33, https://doi.org/10.1139/t79-003, 1979.

833 Wyllie, D. C. and Mah, C. W.: Rock Slope Engineering, 4th ed., Spon, 456 pp., 2004.

834